**CHALMERS**

# Analysis of the Performance of Different $\overline{v^2}$–$f$ Turbulence Models in a Stator Vane Passage Flow

ANDREAS SVENINGSSON

*Department of Thermo and Fluid Dynamics*
CHALMERS UNIVERSITY OF TECHNOLOGY
Göteborg, Sweden, 2003

# Analysis of the Performance of Different $\overline{v^2} - f$ Turbulence Models in a Stator Vane Passage Flow

ANDREAS SVENINGSSON

Department of Thermo and Fluid Dynamics

CHALMERS UNIVERSITY OF TECHNOLOGY

Göteborg, Sweden, 2003

# Analysis of the Performance of Different $\overline{v^2} - f$ Turbulence Models in a Stator Vane Passage Flow

Andreas Sveningsson

Department of Thermo and Fluid Dynamics
Chalmers University of Technology
S-412 96 Göteborg, Sweden
Phone +46-(0)31-7721400
Fax +46-(0)31-180976

This document was typeset using LaTeX.

# Analysis of the Performance of Different $\overline{v^2}-f$ Turbulence Models in a Stator Vane Passage Flow

by

## Andreas Sveningsson

Department of Thermo and Fluid Dynamics
Chalmers University of Technology
SE-412 96 Göteborg, Sweden

## Abstract

When designing the cooling system of modern gas turbines it is important to be able to predict the heat transfer from the hot gas to the walls surrounding the gas path. One flow feature making this rather complicated is the presence of secondary, three-dimensional flow structures, often referred to as horse shoe vortices, which greatly enhance the rate of heat transfer to the endwall, especially in the leading edge region.

During the last few years the $\overline{v^2}-f$ turbulence model has become increasingly popular due to its ability to account for near-wall damping without use of ad hoc damping functions. The $\overline{v^2}-f$ model has also proved to be superior to other RANS methods in many fluid flows where complex flow features are present.

In this study numerical simulations of a well documented stator vane passage flow have been performed using different versions of the $\overline{v^2}-f$ model. The main objective is to investigate the models' ability to predict the secondary fluid motion in the passage between two stator vanes.

The predictions of vane passage flow field using the $\overline{v^2}-f$ model agree well with experiments. It is also shown that this model outperform several commonly used two-equation turbulence models.

As the stator vane flow involves a large stagnation region controlling the stagnation point anomaly, a characteristic deficiency of eddy-viscosity based turbulence models, becomes very important. Therefore, the effect of the realizability constraint is investigated. It is shown that this constraint has a strong impact on the flow, especially in the stagnation region, and improves the predictions of the secondary flow field.

**Keywords:** RANS, stator flow, V2F, realizability, heat transfer

# Acknowledgements

# Nomenclature

## Latin Symbols

| | |
|---|---|
| $a$ | Taylor expansion coefficient; discretization coefficient |
| $b, c$ | Taylor expansion coefficients |
| $A, B, C, D$ | TDMA solver coefficients |
| $C$ | true vane chord |
| $C_1, C_2$ | constants in the $\overline{v^2} - f$ model |
| $C_p$ | static pressure coefficient (cf. Eqn. 4.1) |
| $C_{\varepsilon 1}, C_{\varepsilon 2}$ | constants in the modelled $\varepsilon$ equation |
| $C_\eta, C_{\varepsilon d}$ | constants in the $\overline{v^2} - f$ model |
| $C_{lim}$ | constants in the realizability constraint |
| $C_\mu$ | constant in turbulence model |
| $D$ | divergence term |
| $f$ | relaxation parameter in modelled $\overline{v^2}$ pressure strain rate |
| $H$ | helicity, defined as $H = \omega_i U_i$ |
| $h$ | heat transfer coefficient |
| $k$ | turbulent kinetic energy, defined as $k = \frac{1}{2}\overline{u_i u_i}$ |
| $L$ | turbulent length scale |
| $n$ | unit vector |
| $P$ | vane pitch |
| $P_\phi$ | production rate of $\phi$ |
| $p$ | pressure |
| $Q$ | second invariant of the strain rate tensor |
| $S$ | vane span; source term; $S^2 = S_{ij}S_{ij}$ |
| $S_{ij}$ | symmetric part of the mean strain rate tensor, $S_{ij} = \frac{1}{2}\left(\frac{\partial U_i}{\partial x_j} + \frac{\partial U_j}{\partial x_i}\right)$ |
| $s_{ij}$ | symmetric part of the fluctuating strain rate tensor, $s_{ij} = \frac{1}{2}\left(\frac{\partial u_i}{\partial x_j} + \frac{\partial U_j}{\partial x_i}\right)$ |

| | |
|---|---|
| $St$ | Stanton number, defined as $h/\rho C_p U_{in}$ |
| $T$ | stress tensor |
| $\mathcal{T}$ | turbulent time scale |
| $U$ | mean velocity in $x$-direction |
| $U_i$ | mean velocity in $x_i$-direction |
| $\overline{uv}$ | shear stresses |
| $u$ | fluctuating velocity in $x$-direction |
| $\overline{u^2}$ | normal stress in the $x$-direction |
| $u_i$ | fluctuating velocity in $x_i$-direction |
| $\overline{u_i u_j}$ | Reynolds stress tensor |
| $V$ | mean velocity in $y$-direction; secondary velocity; volume |
| $\mathcal{V}$ | turbulent velocity scale |
| $v$ | fluctuating velocity in $y$-direction |
| $\overline{v^2}$ | normal stress in the wall-normal direction |
| $W$ | mean velocity in $z$-direction |
| $w$ | fluctuating velocity in $z$-direction |
| $\overline{w^2}$ | normal stress in the $z$-direction |

## Greek Symbols

| | |
|---|---|
| $\beta, \beta^\star$ | constants in $k - \omega$ model |
| $\gamma, \gamma^\star$ | constants in $k - \omega$ model; thermodynamic property |
| $\delta$ | boundary layer thickness |
| $\delta_{ij}$ | Kronecker delta |
| $\varepsilon$ | dissipation rate |
| $\varepsilon_{ijk}$ | alternating unit tensor |
| $\eta$ | efficiency; coordinate |
| $\lambda$ | eigenvalue of strain rate tensor |
| $\mu$ | dynamic viscosity |
| $\mu_t$ | dynamic turbulent viscosity |
| $\nu$ | kinematic viscosity |
| $\nu_t$ | kinematic turbulent viscosity |
| $\xi$ | wall-normal coordinate |
| $\rho$ | density |
| $\sigma_\Phi$ | turbulent Prandtl number for variable $\Phi$ |

| | |
|---|---|
| $\phi$ | fluid propoerty; flow angle; pressure-strain rate |
| $\omega$ | specific dissipation ($\propto \varepsilon/k$) |
| $\omega_i$ | vorticity component in $x_i$-direction |

## Subscript

| | |
|---|---|
| $in$ | inlet |
| $E$ | east |
| $e$ | external |
| $W$ | west |
| $ms$ | midspan |
| $w$ | wall |

## Other

| | |
|---|---|
| $\sim$ | indicates an instantaneous quantity |
| $-$ | ensamble average quantity; auto-correlation |

x

# Contents

# Chapter 1

# Introduction to Vane Passage Flows

## 1.1 The need for Gas Turbine Cooling

In the late 1930s the very first gas turbine was developed at the University of Göttingen. After some refinements this engine was soon used to power aircrafts, replacing the comparatively heavy piston engines used at the time. The efficiency of the early gas turbines was relatively low, about 20 %, and since the first prototypes were manufactured it has been a challenge to engineers to improve their performance.

The efficiency of gas turbines of today lie in the range of 35-40 %, a significant improvement since the early days of gas turbine technology, and is still being increased. The prospects of further improvements can be illustrated by analysing a real gas turbine using the Brayton cycle, which is the ideal thermodynamic cycle for gas turbines. The efficiency of this cycle, $\eta_{th}$, is

$$\eta_{th} = 1 - \left( \frac{P_{low}}{P_{high}} \right)^{\gamma/(\gamma-1)} \tag{1.1}$$

where $\gamma > 1$ is a constant and $P_{high}$ and $P_{low}$ are the high and low pressure levels in the ideal cycle. We see that the only way to increase the efficiency is to either lower $P_{low}$ or raise $P_{high}$. As $P_{low}$ depends on the pressure of the surroundings we must raise $P_{high}$ in order to increase the efficiency of the gas turbine, which can be done by increasing the temperature in the gas turbine. Further, increasing the highest temperature in the cycle will increase the power output per unit mass flow, reducing the required *size* (and weight) of the gas turbine, which is of great importance if the turbine is used to power an aircraft. This fact was realised from
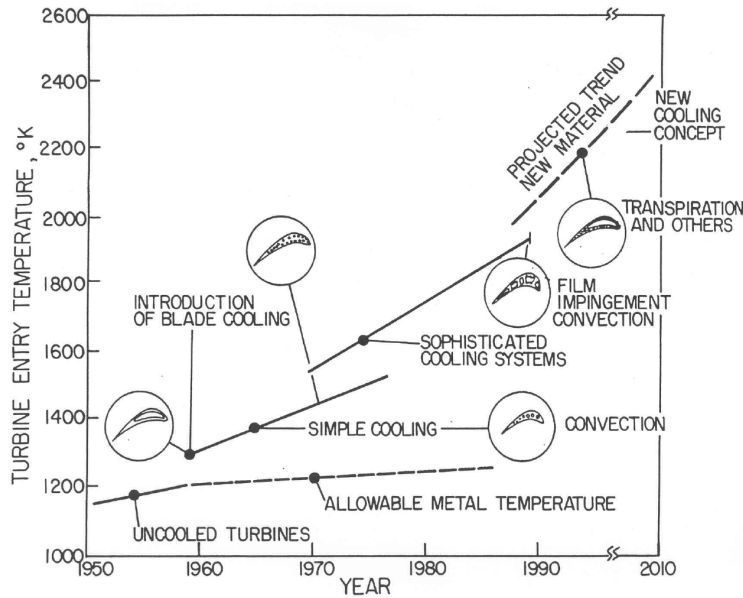
Figure 1.1: Development of gas turbine inlet temperature illustrating the impact of introducing cooling technology.

early on and in Figure 1.1 the increase in turbine inlet temperature since the 1950s is shown.

The major problem with further increasing the highest temperatures in a gas turbine is that the raise in temperature will increase the heat load on the gas turbine hot parts. This increases the thermal stresses within the gas turbine material, which shortens its lifetime and if the temperature is further increased it eventually reaches the melting point of the turbine material. This leaves two possibilities to enhance the performance of the gas turbine, i.e. either to improve the materials in the turbine, so that they can withstand higher temperatures, or to introduce cooling techniques to prevent the temperature of the hot parts from exceeding some critical level. Figure 1.1 reveals the importance the development of increasingly sophisticated cooling designs have had on the maximum allowable turbine inlet temperature. Also included in this figure is a line that shows the potential of increasing the temperature by inventing new materials with improved high temperature properties. Compared to the effect of adding cooling, which decreases the temperature of the hot parts, the effect of raising the maximum allowable *material* temperature is relatively small.

Hence, in order to prolong the life cycle of gas turbines, or to increase their

2

performance, the most efficient route is likely to further develop the turbine cooling technology. For example, reducing the mean section temperature of a rotor blade by $15^oC$ would double its life time expectancy. Also worth mentioning is that the supply of coolant is not for free. It has to be by-passed from the gas turbine compressor and the more coolant removed from the main flow path the lower the overall efficiency. Therefore, the cooling process itself must be as efficient as possible.

Improving gas turbine cooling is all but a trivial matter and requires a thorough understanding of how the complex flow field in the combustor and the first stator/rotor stage develops (these are the regions that require the largest part of the by-passed coolant). Especially, the thermal load on the turbine is important as the first row of stator vanes are hit by an accelerated very hot stream of gas causing the heat transfer in the stagnation region of the vanes to go up. Therefore, methods that accurately predict the characteristics of heat transfer will facilitate the design of the next generation of gas turbines engines.

## 1.2 Why Study Endwall Cooling?

In the previous section it was explained why the temperature in gas turbines is increasing. It was also mentioned that the heat load on the stagnation region of gas turbine stator vanes is, and always has been, profound. Therefore, it is fairly well understood what is required in order to keep the temperature in the stagnation region sufficiently low. Recently, as the energy consumption is continuously going up, the increased environmental awareness has led to legislated requirements of reduced levels of pollutants from energy power plants. A consequence of this seen in the gas turbine community is the trend of using so called low $NO_x$ burners, which substantially reduce the exhaust levels of $NO_x$. A feature of these burners is that the maximum temperature in the combustor must be lowered as most of the $NO_x$ forms in high temperature regions. Reducing the temperature is contradictory to the suggested increase needed to improve the gas turbine performance. The only solution that meet both these requirements is to even out the turbine inlet temperature profile as illustrated in Figure 1.2. One of the consequences this has is that the temperature towards the endwalls of the turbine increases, which in turn enhances the thermal load on the same. This is the reason why lately there has been an increased interest in the flow and heat transfer in the endwall region of gas turbines.
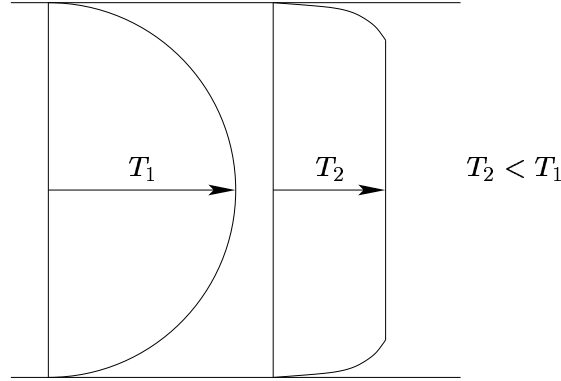
3

$T_1$    $T_2$    $T_2 < T_1$

PSfrag replacements

Figure 1.2: Two turbine inlet temperature profiles showing the trend towards flatter temperature distributions.

## 1.3 The Influence of Secondary Flow Field Structures on Endwall Heat Transfer

One of the primary interests of this study is to investigate the structure of a gas turbine vane passage flow in the vicinity of the endwall/stator vane junction. The reason why the flow in this region is important can be understood by examining the rather complex model of the secondary flow field in Figure 1.3, suggested by Sharma & Butler (1987), that is a result of the interaction between the incoming boundary layer and the stator vane.

From this figure it is easy to imagine that the swirling motion of the secondary structures originating from the stagnation point region, commonly referred to as the horseshoe vortex system, will replace fluid in the incoming boundary layer with fluid from the freestream region. This is important as the boundary layer approaching the stator vane, that has developed in the gas turbine combustor, also has a characteristic temperature profile with cool fluid close to the wall and increasingly warmer fluid away from the wall. This thermal boundary layer can be interpreted as an insulating fluid layer that protects the wall from the very harsh environment in the freestream. When the flow reaches the region of swirling secondary structures the incoming boundary layer is torn apart and the endwall is exposed to fluid in the freestream, which dramatically increases the heat transfer. Also recall, from Figure 1.2, the trend of flattening the inlet temperature profiles, i.e bringing fluid of higher temperature closer to the endwalls.

The secondary motion of this flow is due to the vorticity contained in the
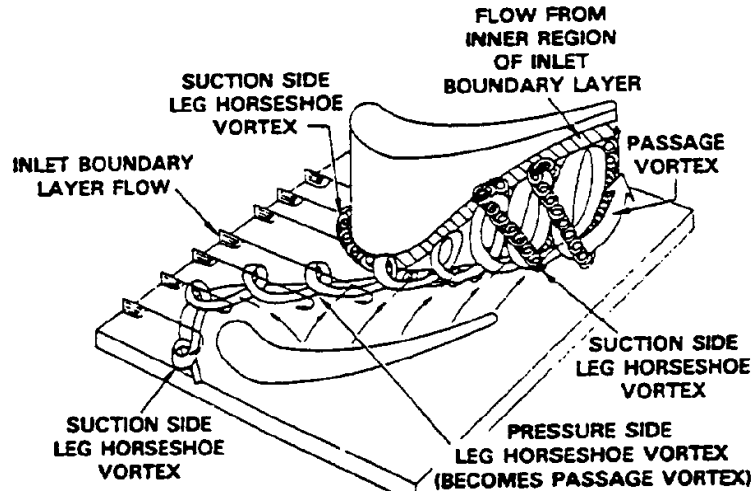
4

Figure 1.3: Secondary flow model by Sharma & Butler (1987).

incoming boundary layer. This vorticity can be thought of as tubes of vorticity rolling along with the boundary layer. When the tubes reach the leading edge of the stators, the stagnation points, they get distorted as the flow in the stagnation region is retarded whereas the the flow between two vanes is accelerated. This distortion will give the tubes the shape of a horseshoe well known from studies of the flow around cylinders.

After the rotating motion has formed it is convected through the passage and experiences the difference in pressure of the pressure and suction side of two adjacent vane profiles. It is this pressure gradient that make the flow turn as it passes through the vane passage (strictly speaking it is vice versa, i.e. the *profile* forces the flow to turn and the associated acceleration is the reason for the pressure difference). The fluid close to the endwall contain slightly less momentum than fluid in the freestream and does therefore change direction more rapidly than fluid away from the wall. This has the effect of moving the pressure side leg of the horseshoe vortex towards the suction side.

Understanding this type of flow is important in turbomachinery design. For example, any attempt to design an effective cooling of the endwall must take into account the fact that the vortices will lift an ejected insulating cool air film away from the endwall material it is supposed to protect. In this case the only effect the coolant will have is to lower the average temperature of the vane passage fluid, i.e. decrease the efficiency of the turbine.

5

# 1.4 Relevant Past Studies

For the last fifty years an excessive amount of research has been invested in the area of gas turbine technology. As discussed in the previous chapter the driving force has been requirements of high efficiency and low emissions. The literature on the subject is vast. The main reason is, of course, that the subject is very difficult as almost all features that make the life of a fluid mechanist hard are present. Some examples are heat transfer itself (both measurements and calculations), three-dimensional flow fields, instationary interactions between stator and blade rows, high temperatures and pressures, transition, strong compressibility effects, high freestream turbulence intensities, streamline curvature, the need for addition of cooling and so on.

In the world of gas turbine research (as in most other) the standard approach is to try to separate as many of these effects as possible from each other and to study them individually. One disadvantage is that when dealing with fluid flows it is difficult to tell what effects that *can* be investigated individually An example from this project could be whether is it relevant or not to draw any conclusions from a CFD analysis on how the secondary flow field distributes film cooling air if the film cooling itself is not included in the analysis. Another more practical problem is that the research area gets split up in many subareas, which makes it difficult to write a review providing an overview of the present research status.

Nevertheless, this section is an attempt. At the very beginning of this project it was not clear which experimental study would be used for the validation of the performance of the turbulence models that were to be studied. Therefore a literature survey of the measurements available at the time was conducted, which is the reason why this section will focus mainly on experimental studies of stator vane flows.

**Measurements and Predictions of Gas Turbine Heat Transfer and Flow Field**

Much of today's understanding of turbine gas path flow field and heat transfer stem from experiments carefully conducted during the latter decades of the nineteenth century. These experiments do not only give the basic understanding of the underlying flow physics but do also form a growing data set that can be used when validating the performance of numerical predictions. As the work presented in this thesis is of numerical nature, well-resolved measurements with documented boundary conditions allowing for a fair comparison with calculations are of high priority. Of particular interest are studies that include the flow adjacent to

turbine endwalls and heat transfer to the same.

The earliest review of the subject is the paper by Sieverding (1985) that summarizes the status of experimental secondary flow research of the time. Of special interest is the discussion on the development of endwall flow models and the physics behind the horseshoe vortex system. One of the conclusions is that the properties of the complex set of vortices depends on the stator vane geometry and that the leading edge effects are closely related to the incidence angle, which suggests variations in the secondary flow field at off design conditions.

Eight years later Simoneau & Simon (1993) review the state of the art in three related areas: configuration-specific experiments, fundamental physics and model development and code development. All these areas are claimed to be needed in order to develop accurate predictive tools for heat transfer in turbine gas paths. A contribution believed to be among the most important is the rotating rig research by Dunn and coworkers at Calspan, e.g. Dunn (1990), Dunn *et al.* (1984). The reasons are high time resolution heat flux measurements obtained using a transient thin-film heat flux gage and that they offer experiments very close to the real world. Also, according to George (2000), this type of heat flux measurements is probably the most reliable method to obtain heat transfer data.

Of greater interest to this work is their review of cascade experiments of which the more important are the work of Langston *et al.* (1977) and Graziani *et al.* (1980) providing a database suited for code validation. A more recent database covering a range of Reynolds numbers was obtained by Boyle & Russell (1990). Simoneau & Simon (1993) also state that the role of the detailed but less realistic cascade experiments is to validate codes and physical models. Also included is a complete list of cascade experiments conducted before 1993.

In the study of Boyle & Russell (1990) local Stanton numbers are determined for Reynolds numbers based on inlet velocity and axial chord between 73,000 and 495,000 using uniform heat flux foil and liquid crystal technique for temperature measurements. One of their conclusions is that the Stanton number patterns are almost independent of both inlet Reynolds number and changes in the inlet boundary thickness and that the secondary flow is stronger for the low Reynolds number cases.

Giel *et al.* (1998) measured endwall heat transfer using the same method as Boyle & Russell (1990) in a rotor cascade. Measurements are obtained for different Mach and Reynolds numbers with and without turbulence grid. Eight different flow conditions were investigated. The endwall heat transfer data presented here, along with the aerodynamic data presented by Giel *et al.* (1996) comprise a complete set of data suitable for CFD code and model validation. Electronic ta-

7

bulations of all data presented in this paper are available upon request. The same research group also measured the blade heat transfer of the same geometry. The results are given in Giel *et al.* (1999). Kalitzin (1999) computed the heat transfer for this experiment using the $\overline{v^2} - f$ and Spalart-Allmaras one-equation turbulence models. It was found that the predictions of the Stanton number show most of the features observed in the experiments but fail to quantitatively predict the heat transfer to the endwall.

Another recent experimental/numerical contribution is the work by Jones and coworkers at University of Oxford. Their annular cascade facility enables short-duration steady flow at engine-like conditions for up to one second to be generated. Spencer & Jones (1996) found that the secondary flow field had greater influence on the casing endwall heat transfer than the hub heat transfer. This was explained with the fact that the hub vortex had lifted from the endwall closer to the leading edge than the casing endwall vortex. Harvey *et al.* (1999) found, quite contradictory to other studies, that the heat transfer rate is strongly influenced by the Reynolds number, an effect that was reproduced in calculations. They also found that the main difference between measurements and calculations is that the secondary flow effects on the endwall are underestimated.

Recently a series of experimental and numerical studies by Thole and coworkes was conducted at Virginia Polytechnic Institute and State University. They investigated the influence of freestream turbulence level and inlet conditions at on the flow field and heat transfer in a large-scale stator vane passage at two Reynolds numbers. One finding was that the vane heat transfer is largely determined by the level of freestream turbulence, showing augmentations of 80% on the pressure side, whereas the heat transfer to the endwall to a greater extent depends on the intensity of the secondary flow field. Further, in Hermanson & Thole (2000*a*) and Hermanson & Thole (2000*b*), the influence of inlet conditions on the secondary flow is illustrated based on numerical investigations. Due to detailed measurements of both flow field and heat transfer being available this set of experiment was chosen as test case for the numerical study in this project and will be described in Section 1.5.

For a more detailed up to date review of gas turbine endwall research including both numerical and experimental investigations see Rubensdörffer (2002).

The influence of turbulence on gas turbine vane heat transfer was investigated by Ames (1997). A range of turbulence scales and intensities was generated at two exit Reynolds numbers and it was found that the turbulence length scale had a significant effect on stagnation region and pressure surface heat transfer. Ames & Plesniak (1997) also examined the effect of turbulence on aerodynamic losses

| | |
|---|---|
| Scaling factor | 9 |
| True chord, $C$ | $59.4 cm$ |
| Pitch, $P$, $/C$ | 0.77 |
| Span, $S$, $/C$ | 0.93 |
| $U_{inlet}$ | $7.33 m/s$ |
| $Re_{in}$ | $2.9 \text{x} 10^5$ |

Table 1.1: Details of the experimental rig.

and wakes. A very interesting study on turbulence effects in gas turbine flows is summarized by Mayle *et al.* (1998). Here it is argued that it is only the turbulence fluctuations of certain frequencies that can affect a boundary layer, and hence, the heat transfer. This suggests that it is not the overall turbulence intensity but the intensity within this frequency range that determines the heat transfer. They also showed that transition is mostly affected by the higher frequencies of turbulence. This has the consequence that capturing both phenomena probably requires separate treatments of different parts of the turbulence energy spectra. Other contributions to this area is work by Arts *et al.* (1990) and Thole *et al.* (1995).

## 1.5   Experimental Test Case for Validation

The experiment chosen for validating the computations carried out in the work is a series of measurements from Virginia Polytechnic Institute and State University, USA, led by Prof. Thole. They provide a detailed set of both flow field and heat transfer measurements including documented inlet profiles, which is rarely found in literature. This group has conducted several experiments at various inlet turbulence intensities and Reynolds numbers on a scaled-up stator vane at low Mach numbers. A summary of their most important findings is given in Thole *et al.* (2002).

In the present thesis only one of the documented experiments, given in Kang & Thole (2000), was numerically investigated. This case is a low turbulence intensity case ($\mathrm{Tu} = 0.6\%$) with an exit Reynolds number of $\mathrm{Re}_{ex} = 1,200,000$. A schematic of the experimental setup is given in Figure 1.4. Additional information is given in Table 1.1. For a detailed description of the rig design see Kang *et al.* (1999).

9

17.8b

Active turbulence
generator grid
b=1.27cm

Window

Splitter plate

Main
flow

17.8b

Plexiglass
wall

Inlet
measurement
location

Y

Z

X

Shaded area shows the
layout of the heater

Trip wire

Boundary
layer
bleed

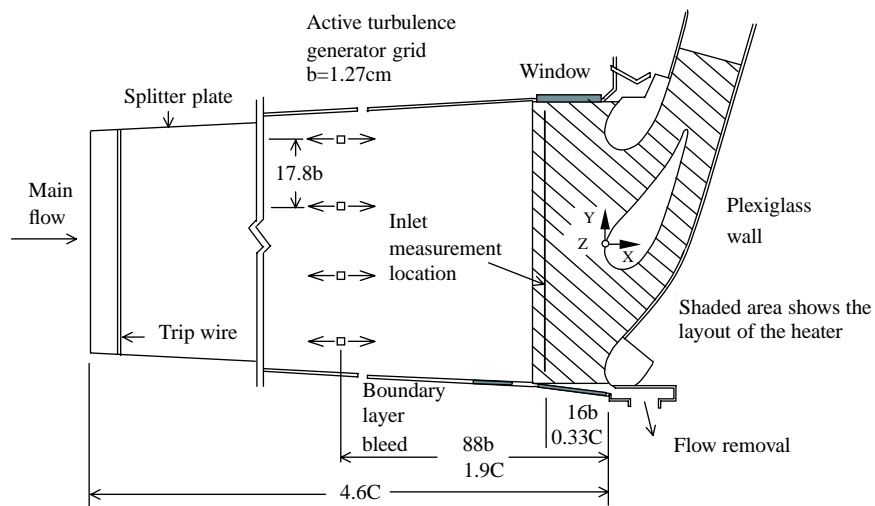88b
1.9C

16b
0.33C

Flow removal

4.6C

Figure 1.4: A schematic of the experimental stator vane test section (Radomsky, 2000).

# Chapter 2

# Governing Equations

## 2.1 Instantaneous Mass and Momentum Conservation Equations

All fluid motion (where the continuum approximation is valid) can be described by the dynamical equations for a fluid

$$\tilde{\rho} \left[ \frac{\partial \tilde{u}_i}{\partial t} + \tilde{u}_j \frac{\partial \tilde{u}_i}{\partial x_j} \right] = -\frac{\partial \tilde{p}}{\partial x_i} + \frac{\partial \tilde{T}_{ij}^{(v)}}{\partial x_j} \tag{2.1}$$

$$\left[ \frac{\partial \tilde{\rho}}{\partial t} + \tilde{u}_j \frac{\partial \tilde{\rho}}{\partial x_j} \right] + \tilde{\rho} \frac{\partial \tilde{u}_j}{\partial x_j} = 0 \tag{2.2}$$

where the tilde symbol indicates that an instantaneous quantity is considered.

For Newtonian fluids the viscous stress tensor can be related to the fluid motion via the molecular viscosity $\mu$

$$\tilde{T}_{ij}^{(v)} = 2\mu \left[ \tilde{s}_{ij} - \frac{1}{3} \tilde{s}_{kk} \delta_{ij} \right], \quad \tilde{s}_{ij} = \frac{1}{2} \left( \frac{\partial \tilde{u}_i}{\partial x_j} + \frac{\partial \tilde{u}_j}{\partial x_i} \right) \tag{2.3}$$

For incompressible fluids any derivative of $\tilde{\rho}$ is zero and Eqn. 2.2 directly gives $\partial \tilde{u}_j / \partial x_j = 0$, so that the dynamic equations can be simplified leading to

$$\left[ \frac{\partial \tilde{u}_i}{\partial t} + \tilde{u}_j \frac{\partial \tilde{u}_i}{\partial x_j} \right] = -\frac{1}{\rho} \frac{\partial \tilde{p}}{\partial x_i} + \nu \frac{\partial^2 \tilde{u}_i}{\partial x_j^2} \tag{2.4}$$

$$\frac{\partial \tilde{u}_j}{\partial x_j} = 0 \tag{2.5}$$

11

After the viscous stresses being closed using Newton's ansatz we have a system of four equations involving four unknown variables. Assuming a complete set of boundary conditions being available the system of equations can be directly solved without any further modelling. This approach is called Direct Numerical Simulation (DNS). However, for turbulent (or transitional) flows the size of the turbulent flow structures will cover a large spectra ranging from the tiny Kolmogorov scales to scales comparable to the size of physical flow domain. A numerical simulation that resolves this scale separation will require enormous amounts of computer power and will not be possible for industrial flows in a foreseeable future.

## 2.2 Averaged Mass and Momentum Conservation Equations

As mentioned in the previous section resolving instantaneous turbulent fluctuations in flows of industrial importance is not yet possible. However, industry today use numerical simulations of extremely complex fully turbulent flows as an everyday design tool. How is this possible? The answer is that in most applications the turbulence itself is of secondary interest, only its effect on the mean flow characteristics such as, for example, the overall drag of a car is important. This allows for computations where the turbulent fluctuations can be accounted for using statistical measures of turbulence. This means that we represent the fluctuations with some kind of averaged quantity and try to find out how this quantity is coupled to the mean flow and how to calculate it without having to resolve all the small scales of turbulence. In this and the following sections this (unknown) coupling between the turbulence and the mean flow is derived and some methods of calculating it are discussed.

The instantaneous motion introduced above is decomposed into an average (ensamble) and a fluctuating component

$$
\begin{aligned}
\tilde{u}_i &= U_i + u_i \\
\tilde{p} &= P + p
\end{aligned}
$$

(2.6)

Inserting these expressions into the instantaneous equations and averaging yields the Reynolds Average Navier-Stokes equation (hereafter referred to as the RANS

equation) for the ensamble averaged motion

$$\left[\frac{\partial U_i}{\partial t} + U_j \frac{\partial U_i}{\partial x_j}\right] = -\frac{1}{\rho}\frac{\partial P}{\partial x_i} + \nu \frac{\partial^2 U_i}{\partial x_j^2} - \frac{\partial}{\partial x_j}\overline{u_i u_j} \qquad (2.7)$$

$$\frac{\partial U_j}{\partial x_j} = 0 \qquad (2.8)$$

During this procedure we have averaged out all effects the stochastic (or at least chaotic) turbulent fluid motion has on the *average* flow field and represented it by the additional term $\partial/\partial x_j \overline{u_i u_j}$, named the Reynolds stress. This is the unknown statistical term mentioned above that, if properly closed, will enable great savings in terms of computational requirements as it includes the effect on the mean flow of all the turbulent flow structures allowing for simulations of complex fluid flows. Unfortunately one big issue remains. The averaging process applied above generated in total six unknown variables (the symmetric Reynolds stress tensor) that somehow must be related to other *known* variables in order to obtain a closed system of equations. The modelling of the Reynolds stress tensor has been one of the largest research areas in computational fluid dynamics during the last thirty years. In the following section some of the suggested closures, in particular the so called eddy-viscosity based closures, will be discussed.

## 2.3 Turbulence Modelling — Eddy Viscosity

As mentioned above the area of turbulence modelling is very large. Therefore this section will focus on the modelling approach used in this project, the modelling of the Reynolds stress tensor based on the concept of eddy viscosity. The name eddy viscosity origins from the model being a direct analogy to the modelling of the viscous stress tensor as given in Eqn. 2.3.

In a turbulent flow the *generation* of Reynolds stresses is proportional to the mean rate of strain. If we assume that the turbulence responds rather quickly to changes in the mean flow we would expect the Reynolds stresses themselves to be related to the mean rate of strain. This means that large Reynolds stresses will generally be found in areas of high strain, which most likely makes it easier to find an accurate empirical formula for the ratio of a Reynolds stress to the mean rate of strain than a model of the Reynolds stress itself. In fact, the quantity eddy viscosity is defined as this ratio, i.e. the ratio between the Reynolds stress tensor

13

and the mean rate of strain, which in the most general case reads

$$-\overline{u_i u_j} = \nu_{t,ijlm} \left( \frac{\partial U_l}{\partial x_m} + \frac{\partial U_m}{\partial x_l} \right) - \frac{2}{3} k \delta_{ij} \qquad (2.9)$$

Since this expression involves a summation over indices we cannot write this definition as a ratio of the turbulent stresses and the strain rate but in the following discussion $\nu_t$ is interpreted as this ratio. Now we have an unknown 4:th order tensor to model for the RANS equation to be closed (using certain properties of this tensor the number of unknowns can be reduced to the order of 50 (Johansson, 2002), which is still too high for being of any practical use). In order to reduce the number of unknowns we assume that we can neglect all out-of-plane contributions. The simplified expression reads

$$-\overline{u_i u_j} = \nu_{t,ij} \left( \frac{\partial U_i}{\partial x_j} + \frac{\partial U_j}{\partial x_i} \right) - \frac{2}{3} k \delta_{ij} \qquad (2.10)$$

(no summation on $i$ and $j$) and we are down to six unknown eddy viscosities. In the process we probably lost important information about the flow but arrived at an acceptable number of eddy viscosities to close. Unfortunately the viscosities are related to each other in a manner that would be difficult to describe in general. For further discussion on this subject see Bradshaw (1996). Hence, the most commonly used assumption is to treat the eddy viscosity as a scalar quantity given by

$$\nu_t = C_\mu \mathcal{V}^2 \mathcal{T} \qquad (2.11)$$

where $\mathcal{V}$ and $\mathcal{T}$ are a turbulent velocity scale and a turbulent time scale, respectively. $C_\mu$ is supposed to be a universal constant and the Reynolds stresses can be calculated using

$$\overline{u_i u_j} = -2\nu_t S_{ij} + \frac{2}{3} k \delta_{ij} \qquad (2.12)$$

Recall, from its definition, that the eddy viscosity is the ratio of the *turbulent* stress $\overline{u_i u_j}$ and the *mean flow* velocity gradient. Here we have assumed that we can obtain the eddy viscosity using two local turbulent scales (Eqn. 2.11) that only have implicit connections to the mean flow, whereas the stress and the strain rate in Eqn. 2.10 are different types of quantities (Bradshaw, 1996).

In this section we have replaced (modelled) the unknown Reynolds stresses with the scalar eddy viscosity times a velocity gradient. The scalar eddy viscosity

in turn was modelled using turbulent velocity and time scales. Of course these scales are unknown too, and the following sections give some examples of how they can be estimated from (known) mean flow variables using transport equations for turbulent quantities.

### 2.3.1   Standard $k - \varepsilon$ Model

The number of $k - \varepsilon$ turbulence models that can be found in literature is vast. The standard high Reynolds number $k - \varepsilon$ model given in e.g. Jones & Launder (1972) has been followed by many versions that most often outperform the original. The main reason why it is given here is that it forms the basis of the more advanced $\overline{v^2} - f$ model described in Section 2.3.3, which is used extensively in this work. This model has also been used to generate initial solutions to the $\overline{v^2} - f$ computations.

The $k - \varepsilon$ turbulence model is based upon the exact transport equations for the turbulent kinetic energy $k$ and its dissipation rate $\varepsilon$ (the derivation of the $k$ equation can be found in Wilcox (1993) where also the derivation of the $\varepsilon$ equation is outlined). $k^{1/2}$ directly gives the velocity scale needed to close Eqn. 2.11. To get the time scale we can use the same velocity scale together with a length scale, i.e. $\mathcal{T} = L/k^{1/2}$. This length scale is in $k - \varepsilon$ models given by $L = k^{3/2}/\varepsilon$, hence the $\varepsilon$ equation is sometimes referred to as a length-scale determining equation. Several CFD researches have suggested transport equations for different combinations of $k^m L^n$ in order to determine the turbulent length scale (once the new quantity is known $L$ can be resolved), cf. Wilcox (1993).

The modelled $k$ and $\varepsilon$ equations read

$$\frac{\partial k}{\partial t} + u_j \frac{\partial k}{\partial x_j} \;\; = \;\; \frac{\partial}{\partial x_j}\left(\left(\nu + \frac{\nu_t}{\sigma_k}\right)\frac{\partial k}{\partial x_j}\right) + P_k - \varepsilon \tag{2.13}$$

$$\frac{\partial \varepsilon}{\partial t} + u_j \frac{\partial \varepsilon}{\partial x_j} \;\; = \;\; \frac{\partial}{\partial x_j}\left(\left(\nu + \frac{\nu_t}{\sigma_\varepsilon}\right)\frac{\partial \varepsilon}{\partial x_j}\right) + \frac{C_{\varepsilon 1}P_k - C_{\varepsilon 2}\varepsilon}{\mathcal{T}} \tag{2.14}$$

Near walls $\mathcal{T}$ goes to zero causing a singularity in the $\varepsilon$ equation. To avoid numerical problems due to this singularity Durbin (1991) suggested a lower bound on the time scale using the Kolmogorov variables, $\mathcal{T} \geq 6\sqrt{\nu/\varepsilon}$. However, this modification was never implemented for the standard $k - \varepsilon$ computations.

The $\varepsilon$ wall boundary condition, which will be derived in Section 2.3.4, reads

$$\varepsilon \to 2\nu \frac{k}{y^2} \qquad \text{as } y \to 0 \tag{2.15}$$

15

In this and the following sections the notation in Eqn. 2.16 is frequently used

$$P_k = 2\nu_t S^2, \quad S^2 = S_{ij} S_{ij}, \quad S_{ij} = \frac{1}{2} \left( \frac{\partial U_i}{\partial x_j} + \frac{\partial U_j}{\partial x_i} \right) \tag{2.16}$$

where $P_k$ is the production of turbulent kinetic energy, i.e. a measure of the rate of conversion of mean flow kinetic energy into turbulence kinetic energy. In reality this process can also take place in the reversed direction ("negative" production) but the assumptions made when deriving the scalar eddy viscosity (with constant $C_\mu$) only allow for energy transport in one direction.

The standard $k - \varepsilon$ model coefficients are

$$C_\mu = 0.09, \quad C_{\varepsilon 1} = 1.44, \quad C_{\varepsilon 2} = 1.92, \quad \sigma_k = 1.0, \quad \sigma_\varepsilon = 1.3 \tag{2.17}$$

## 2.3.2 Standard $k - \omega$ Model

The $k - \omega$ model used in this work is the original model suggested by Wilcox (1988) commonly referred to as the standard $k - \omega$ turbulence model. The turbulent scales in the eddy viscosity relation are $\mathcal{V} = k^{1/2}$ and $\mathcal{T} = 1/\omega$. As for the standard $k - \varepsilon$ model the exact $k$-equation is modelled and a new transport equation for the quantity $\omega$, named the specific dissipation rate, is derived (cf. the comment on length scale determining in the previous section, here $\omega = k^{1/2} L^{-1}$). $\omega$ is related to the dissipation rate via

$$\omega = \frac{\varepsilon}{\beta^\star k} \tag{2.18}$$

The modelled $k$ and $\omega$ equations using the original notation read

$$\frac{\partial k}{\partial t} + u_j \frac{\partial k}{\partial x_j} = \frac{\partial}{\partial x_j} \left( (\nu + \sigma^\star \nu_t) \frac{\partial k}{\partial x_j} \right) + P_k - \beta^\star \omega k \tag{2.19}$$

$$\frac{\partial \omega}{\partial t} + u_j \frac{\partial \omega}{\partial x_j} = \frac{\partial}{\partial x_j} \left( (\nu + \sigma \nu_t) \frac{\partial \omega}{\partial x_j} \right) + \gamma \frac{\omega}{k} P_k - \beta \omega^2 \tag{2.20}$$

$$\nu_t = \gamma^\star \frac{k}{\omega} \tag{2.21}$$

$$\beta = 3/40, \quad \beta^\star = 9/100, \quad \gamma = 5/9, \quad \gamma^\star = 1, \quad \sigma = 1/2, \quad \sigma^\star = 1/2 \tag{2.22}$$

16

and the wall boundary condition for $\omega$ is

$$\omega \to \frac{6\nu}{\beta y^2} \qquad \text{as } y \to 0 \qquad (2.23)$$

The only flow *variable* in this expression is $\nu$. As $\nu$ too is constant this boundary condition is numerically appealing as the value of $\omega$ at the first interior node depends on the mesh only. Herein lies an important difference from e.g. $k - \varepsilon$ and $\overline{v^2} - f$ models, which sometimes have strong variable couplings at wall boundaries that can cause numerical difficulties. This issue will be further addressed in Section 2.3.4.

### 2.3.3 $\overline{v^2} - f$ **Models**

During the last few years the $\overline{v^2} - f$ turbulence model, originally suggested by Durbin, has become increasingly popular due to its ability to account for near-wall damping without use of damping functions. The $\overline{v^2} - f$ model has also shown to be superior to other RANS methods in many fluid flows where more complex flow features are present, e.g. separation in an asymmetric diffuser (Iaccarino, 2001). The advantages of the model have attracted quite a few CFD researchers and several of them have suggested modifications to the original model leading to a set of different $\overline{v^2} - f$ models. In this work three of the proposed $\overline{v^2} - f$ models are compared. They will hereafter be labelled Model 1–3 and are given below.

**Physical Background**

All $\overline{v^2} - f$ turbulence models of today are based on the standard $k - \varepsilon$ model (i.e. no low-Reynolds number extensions) and $k$ and $\varepsilon$ are used to form the turbulent time scale, $\mathcal{T}$. The $\overline{v^2} - f$ model differs from the family of two-equation models in that here a modelled wall normal Reynolds stress component, labelled $\overline{v^2}$, is used as the turbulent velocity scale, $\mathcal{V} = (\overline{v^2})^{1/2}$, i.e. not the usual $k^{1/2}$. This has the implication that we must solve an additional transport equation for the wall normal stress, which in turn needs another flow field parameter, $f$, that too is governed by a partial differential equation. All in all, the $\overline{v^2} - f$ model requires solving the standard $k - \varepsilon$ equations together with the additional $\overline{v^2}$ and $f$ equations. This, of course, increases the computational requirements by some 30% as we must find solutions to, in total, nine instead of seven partial differential equations.

The justification for the increased computational cost can be exemplified by considering a fully developed turbulent wall boundary layer. By inspecting the

17

mean flow momentum equation we see that the only Reynolds stress component felt by the mean flow is the shear stress $\overline{uv}$. Hence, in order to predict the mean flow we must have a sufficiently good model for this stress component. Using the scalar eddy-viscosity approach outlined in Section 2.3 the modelled shear stress component is calculated according to

$$-\overline{uv} = C_\mu \mathcal{V}^2 \mathcal{T} \frac{dU}{dy} \tag{2.24}$$

From the exact transport equation for $\overline{uv}$ the production rate of $\overline{uv}$, $P_{\overline{uv}}$, is given by

$$P_{\overline{uv}} = -\overline{v^2} \frac{dU}{dy} \tag{2.25}$$

As no other term is taken into account in eddy-viscosity modelling we assume that the shear stress itself divided by some typical turbulent time scale will be proportional to $P_{\overline{uv}}$

$$\frac{\overline{uv}}{\mathcal{T}} \sim P_{\overline{uv}} \tag{2.26}$$

Hence,

$$\overline{uv} \sim \mathcal{T} P_{\overline{uv}} = -\overline{v^2} \mathcal{T} \frac{dU}{dy} \tag{2.27}$$

which is exactly the expression in Eqn. 2.24 if the constant of proportionality is $C_\mu$ and the velocity scale is chosen to be $\overline{v^2}^{(1/2)}$. Hereby it has been shown that the proper velocity scale to base the eddy-viscosity model upon in order to correctly model the shear stress in a fully developed channel flow must be $\overline{v^2}^{(1/2)}$.

The standard estimate for the velocity scale is the turbulent kinetic energy, $k^{(1/2)}$. In Section 2.3.4 it will be shown that in the vicinity of solid walls $k \sim y^2$ and $\overline{v^2} \sim y^4$, i.e. the damping of the wall normal component $\overline{v^2}$ is much stronger than the damping of $k$ due to the kinematic blocking of the wall. Therefore models with velocity scales based on $k^{(1/2)}$ are in general expected to give worse predictions of the $\overline{uv}$ behavior close to walls than if the scale is $\overline{v^2}^{(1/2)}$.

In Figure 2.1 the normalized eddy-viscosity is plotted for DNS data (Moser *et al.*, 1999). The DNS eddy-viscosity was computed according to its definition, $\nu_t = -\overline{uv}/\frac{dU}{dy}$, whereas the $k - \varepsilon$ and $\overline{v^2} - f$ eddy-viscosities were obtained from
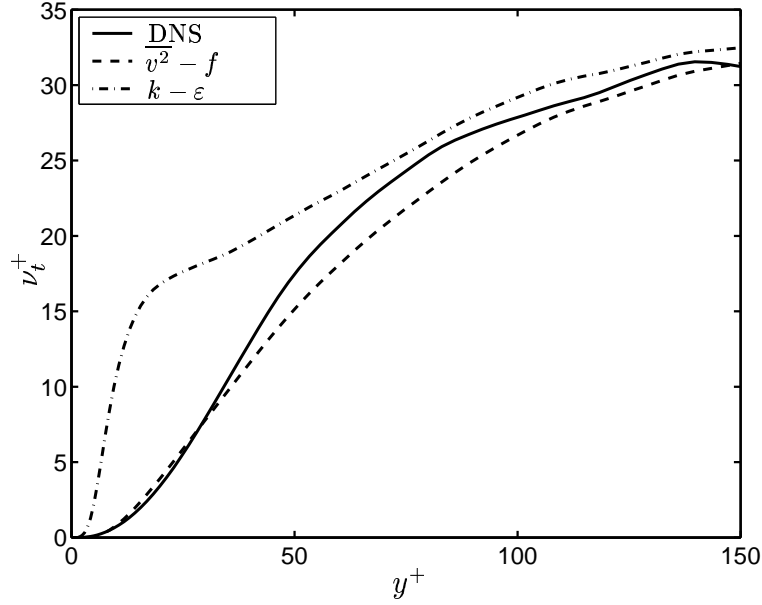
18

Figure 2.1: Normalized turbulent viscosity for different $\nu_t$ closures computed from DNS data

$\nu_t = C_\mu k^2/\varepsilon$ and $\nu_t = C_\mu \overline{v^2} k/\varepsilon$, respectively. Clearly, as pointed out by Durbin (1991), the standard $k - \varepsilon$ model fails to reproduce the true eddy-viscosity simply because the $y$-dependence of $k^2/\varepsilon$ is wrong (in low-Reynolds number $k - \varepsilon$ models this is fixed by introducing a damping function defined as the ratio between $C_\mu k^2/\varepsilon$ and $\nu_t$). From Figure 2.1 we also see that if we somehow have the $\overline{v^2}$ distribution we can get a very good estimate of $\nu_t$, especially in the important near-wall region, without use of damping functions.

Now we introduce a new transport equation for an imaginary stress component $\overline{v^2}$ that is always normal to the closest wall so that the ideas from the channel flow case can be applied to more complex geometries. Note that for the whole idea to work the $\overline{v^2}$ equation must somehow be sensitized to the distance to the nearest wall in order to account for the kinematic wall damping. A modelled equation for the wall normal Reynolds stress component can be obtained using the exact

19

Reynolds stress transport equation as starting point.

$$\frac{\partial \overline{v^2}}{\partial t} + U_j \frac{\partial \overline{v^2}}{\partial x_j} = \underbrace{-\frac{2}{\rho}\overline{p\frac{\partial v}{\partial y}}}_{\phi_{22}} \underbrace{- 2\overline{vu_j}\frac{\partial V}{\partial x_j}}_{P_{22}} \underbrace{- 2\nu\overline{\frac{\partial v}{\partial x_j}\frac{\partial v}{\partial x_j}}}_{\varepsilon_{22}}$$

$$+ \underbrace{\frac{\partial}{\partial x_j}\left[-\frac{2}{\rho}\overline{pv}\delta_{2j} - \overline{v^2 u_j} + \nu\frac{\partial \overline{v^2}}{\partial x_j}\right]}_{D_{22}} \quad (2.28)$$

where the four right hand side terms in turn are: pressure-strain ($\phi_{22}$), production ($P_{22}$), dissipation ($\varepsilon_{22}$) and divergence ($D_{22}$) terms.

As the equation we look for must be independent of the chosen coordinate direction the terms in the Reynolds stress equation have to be simplified. Returning to the turbulent boundary layer example it is seen that the mean flow kinetic energy is transformed to turbulence kinetic energy by the shear stress component via $\overline{uv}$ acting on the mean flow gradient $\partial U/\partial y$; all the turbulent kinetic energy produced enters the streamwise Reynolds stress component. We also know that turbulence in fact is three-dimensional and that the other two Reynolds stress components then must get energy from the streamwise component. This redistribution of turbulence energy is mainly due to the so called pressure-strain term. Hence, for a turbulent boundary layer there will be no production of turbulent kinetic energy in the wall normal component. This component will receive energy from the pressure-strain term only, which we need to model.

As is the case for most eddy-viscosity turbulence models all the divergence terms are modelled using an eddy-diffusivity approximation, i.e.

$$\frac{\partial}{\partial x_j}\left[-\frac{2}{\rho}\overline{pv}\delta_{2j} - \overline{v^2 u_j}\right] \approx \frac{\partial}{\partial x_j}\left[\frac{\nu_t}{\sigma_k}\frac{\partial \overline{v^2}}{\partial x_j}\right] \quad (2.29)$$

The terms left to model are the dissipation rate and the pressure-strain terms. In the $\overline{v^2} - f$ model they are both included in the $\overline{v^2}$ equation source term $kf$, defined as

$$kf \equiv \phi_{22} - \varepsilon_{22} + \frac{\overline{v^2}}{k}\varepsilon \quad (2.30)$$

where the last term is cancelled by a sink term in the $\overline{v^2}$ equation, the modelled dissipation rate of $\overline{v^2}$ (cf. Eqn 2.31). This cancellation makes the choice of the

20

additional term somewhat arbitrary, which has been used when modifying the original $\overline{v^2} - f$ model, eg. Lien & Kalitzin (2001). One can also interpret $\varepsilon_{22} - \varepsilon \overline{v^2}/k$ as the difference in exact and modelled dissipation rate.

The ideas described in short above led to a modelled $\overline{v^2}$ equation, suggested by Durbin (1991, 1993, 1995$b$), on the following form

$$\frac{\partial \overline{v^2}}{\partial t} + u_j \frac{\partial \overline{v^2}}{\partial x_j} = \frac{\partial}{\partial x_j}\left(\left(\nu + \frac{\nu_t}{\sigma_k}\right)\frac{\partial \overline{v^2}}{\partial x_j}\right) + kf - \frac{\overline{v^2}}{k}\varepsilon \qquad (2.31)$$

This equation is just a modelled transport equation for an imaginary wall normal Reynolds stress component. By first sight there is no evidence of how this equation can have any of the near wall properties we wanted it to have. The key is the flow variable $f$, which is governed by a modified Helmholtz equation of elliptic nature.

$$L^2 \frac{\partial^2 f}{\partial x_j^2} - f = \underbrace{\frac{C_1}{T}\left(\frac{\overline{v^2}}{k} - \frac{2}{3}\right)}_{\phi_{22,S}} \underbrace{-C_2 \frac{P_k}{k}}_{\phi_{22,R}} - \frac{1}{T}\left(\frac{\overline{v^2}}{k} - \frac{2}{3}\right) \qquad (2.32)$$

As $kf$ is the modelled effect of the pressure-strain term, $\phi_{22}$, in the $\overline{v^2}$ equation $f$ can be interpreted as $\phi_{22}/k$. In Launder *et al.* (1975) different models for $\phi_{ij}$ are discussed. The terms $\phi_{22,S}$ and $\phi_{22,R}$ in Eqn. 2.32 are the so called slow and rapid pressure-strain terms discussed in this paper. The last term on the right hand side was added to ensure the correct farfield behaviour, whereas the ellipticity is introduced via the left hand side differential operator.

Modelling the pressure-strain term (and the difference in exact and modelled dissipation rate) in the $\overline{v^2}$ equation with $kf$ is argued to in part account for the non-local kinematic blocking of the wall normal stress component. This important feature of wall bounded turbulent flows is usually not captured using single point closure models without use of ad hoc damping functions. Note that the pressure in a fluid flow is of elliptic nature and therefore the correlation of fluctuating pressure and fluctuating velocity gradient (the pressure-strain) is also elliptic. A thorough discussion on this subject is given in Manceau *et al.* (2001), who investigated how pressure-strain is affected by inhomogeneity and anisotropy.

**Model 1**

This version of the $\overline{v^2} - f$ model is given in Parneix *et al.* (1998) and is similar to the very first $\overline{v^2} - f$ models, e.g. Durbin (1991). The $\overline{v^2}$ and $f$ equations are

21

given in Eqn. 2.31 and 2.32. As is the case for all $\overline{v^2} - f$ models it is based on the standard $k$ and $\varepsilon$ equations (2.13,2.14) and the eddy viscosity is obtained from

$$\nu_t = C_\mu \overline{v^2} T \tag{2.33}$$

where the turbulent time scale, $T$, and length scale, $L$, are given by

$$\mathcal{T} = \max\left(\frac{k}{\varepsilon}, 6\sqrt{\frac{\nu}{\varepsilon}}\right) \tag{2.34}$$

$$L = C_L \max\left(\frac{k^{3/2}}{\varepsilon}, C_\eta \frac{\nu^{3/4}}{\varepsilon^{1/4}}\right) \tag{2.35}$$

The limits, expressed in Kolmogorov variables, are introduced in order to avoid singularities in the governing equations at solid walls and are active only very close to walls ($y^+ < 5$). The only modification to the $k$ and $\varepsilon$ equations (except for the time scale constraint above) is that the "constant" $C_{\varepsilon 1}$ is dampened close to walls according to

$$C_{\varepsilon 1} = 1.4\left(1 + C_{\varepsilon d}\sqrt{\overline{v^2}/k}\right) \tag{2.36}$$

The wall boundary conditions for this model are $U_j = k = \overline{v^2} = 0$, $\overline{v^2} = \mathcal{O}(y^4)$ and, from Taylor expansion, $\varepsilon/\nu \to 2k/y^2$ as $y$ approaches zero, $y$ being the normal distance to the nearest wall. The latter two conditions result in the following boundary conditions for $\varepsilon$ and $f$

$$\varepsilon = 2\nu\left(\frac{k}{y^2}\right); \quad f = \frac{-20\nu^2}{\varepsilon}\left(\frac{\overline{v^2}}{y^4}\right) \tag{2.37}$$

The model constants are given in Table 2.1.

**Model 2**

The originally suggested $\overline{v^2} - f$ model suffer from being numerically unstable due to the strong coupling of $f$, $\overline{v^2}$ and $\varepsilon$ in the $f$ wall boundary condition. Strong variable coupling can be dealt with using so called coupled solvers, which will be described in Section 3.4.2. In order to make the $\overline{v^2} - f$ model suitable for segregated (decoupled) solvers Lien & Kalitzin (2001) modified the model so that the $f$ wall boundary condition becomes much more numerically attractive.

One way, probably the easiest, to derive the boundary condition for $f$ is to start with the definition of $kf$, which reads

$$kf \equiv \phi_{22} - \varepsilon_{22} + \frac{\overline{v^2}}{k}\varepsilon \tag{2.38}$$

The behaviour of $\phi_{22}$ and $\varepsilon_{22}$ near walls is (Mansour *et al.* (1988))

$$\phi_{22} \to -2\frac{\overline{v^2}}{k}\varepsilon, \quad \varepsilon_{22} \to 4\frac{\overline{v^2}}{k}\varepsilon \quad \text{as } y \to 0 \tag{2.39}$$

When this is used in Eqn. 2.38 we immediately get the boundary condition for $f$

$$kf \to -2\frac{\overline{v^2}}{k}\varepsilon - 4\frac{\overline{v^2}}{k}\varepsilon + \frac{\overline{v^2}}{k}\varepsilon = -5\frac{\overline{v^2}}{k}\varepsilon \quad \text{as } y \to 0 \tag{2.40}$$

i.e.

$$f \to -5\frac{\overline{v^2}}{k^2}\varepsilon \to \frac{-20\nu^2}{\varepsilon}\frac{\overline{v^2}}{y^4} \quad \text{as } y \to 0 \tag{2.41}$$

where the asymptotic behaviour of $\varepsilon \to 2\nu k/y^2$, has been used to replace $k$.

Lien & Kalitzin (2001) redefined $kf$ as

$$kf \equiv \phi_{22} - \varepsilon_{22} + 6\frac{\overline{v^2}}{k}\varepsilon \tag{2.42}$$

in order to make $kf \to 0$ as $y \to 0$ (cf. Eqn. 2.40), which is a more stable boundary condition than the original. This means that we have to change the modelled dissipation rate in the $\overline{v^2}$ equation to $-6\varepsilon\overline{v^2}/k$ in order to cancel the change in the definition of $kf$. Hence, also the modelled production term, $kf$, must be modified. This was done by introducing some changes in the $f$ equation in a way that maintained both the near-wall and the farfield properties of the original model. The new $\overline{v^2}$ and $f$ equations read

$$\frac{\partial \overline{v^2}}{\partial t} + u_j\frac{\partial \overline{v^2}}{\partial x_j} = \frac{\partial}{\partial x_j}\left(\left(\nu + \frac{\nu_t}{\sigma_k}\right)\frac{\partial \overline{v^2}}{\partial x_j}\right) + kf - 6\overline{v^2}\frac{\varepsilon}{k} \tag{2.43}$$

$$L^2\frac{\partial^2 f}{\partial x_j^2} - f = \frac{C_1}{T}\left(\frac{\overline{v^2}}{k} - \frac{2}{3}\right) - C_2\frac{P_k}{k} - \frac{1}{T}\left(6\frac{\overline{v^2}}{k} - \frac{2}{3}\right) \tag{2.44}$$

and the only additional changes to Model 1 are the $f$ wall boundary condition and a new set of model constants that are given in Table 2.1.

23

In the farfield the elliptic operator $\partial^2 f / \partial x_j^2$ is assumed to be negligible (in fact, Davidson *et al.* (2003) showed that this is not the case even for fully developed channel flow) and the $f$ equations reduce to

$$-f = \frac{C_1}{T} \left( \frac{\overline{v^2}}{k} - \frac{2}{3} \right) - C_2 \frac{P_k}{k} - \frac{1}{T} \left( \frac{\overline{v^2}}{k} - \frac{2}{3} \right)$$

$$-f = \frac{C_1}{T} \left( \frac{\overline{v^2}}{k} - \frac{2}{3} \right) - C_2 \frac{P_k}{k} - \frac{1}{T} \left( 6 \frac{\overline{v^2}}{k} - \frac{2}{3} \right) \quad (2.45)$$

for Model 1 and 2, respectively. In order to see that Model 1 and 2 give exactly the same farfield source term in the $\overline{v^2}$ equation use Eqn. 2.45 for $f$ in the $\overline{v^2}$ equations (Eqn. 2.31 and 2.43). The source term in both cases is

$$-C_1 \frac{\epsilon}{k} \left( \overline{v^2} - \frac{2}{3} k \right) + C_2 P_k - \frac{2}{3} \epsilon \quad (2.46)$$

The near-wall region behaviour of the models is harder to compare as the value of $f$ in Model 2 has been "offset" so that $f_{wall} = 0$. However, except for the offset, the near-wall variable dependence of the $\overline{v^2}$ and $f$ equations is the same as the only difference is whether $\overline{v^2}/k$, which is of order $\mathcal{O}(y^2)$ (i.e. practically zero close to walls), should by multiplied by 1 or 6. Hence, only the model constants alter the near-wall results.

**Model 3**

The third and final $\overline{v^2} - f$ model investigated in this work is given in Kalitzin (1999) and is very similar to Model 2. The $\overline{v^2}$ and $f$ equations for Model 3 read

$$\frac{\partial \overline{v^2}}{\partial t} + u_j \frac{\partial \overline{v^2}}{\partial x_j} = \frac{\partial}{\partial x_j} \left( \left( \nu + \frac{\nu_t}{\sigma_k} \right) \frac{\partial \overline{v^2}}{\partial x_j} \right) + k f - 6 \overline{v^2} \frac{\varepsilon}{k} \quad (2.47)$$

$$L^2 \frac{\partial^2 f}{\partial x_j^2} - f = \frac{C_1}{T} \left( \frac{\overline{v^2}}{k} - \frac{2}{3} \right) - C_2 \frac{P_k}{k} - \frac{1}{T} \left( 5 \frac{\overline{v^2}}{k} - 0 \right) \quad (2.48)$$

This model's set of constants is given in Table 2.1. Note that the constant $C_1$ of Model 3 can be written as

$$C_{1 \ Model3} = C_{1 \ Model2} - 1 \quad (2.49)$$

If this relation is inserted in the $f$ equation for Model 3 it can be shown that this equation is identical to the $f$ equation of Model 2. Hence, the only difference of Model 2 and 3 is a retuning of the two model constants $C_\mu$ and $C_{\epsilon d}$.

24

| Constant | Model 1 | Model 2 | Model 3 |
|:---:|:---:|:---:|:---:|
| $C_\mu$ | 0.22 | 0.22 | 0.19 |
| $C_{\varepsilon d}$ | 0.045 | 0.050 | 0.045 |
| $C_{\varepsilon 2}$ | 1.9 | 1.9 | 1.9 |
| $C_1$ | 1.4 | 1.4 | 0.4 |
| $C_2$ | 0.3 | 0.3 | 0.3 |
| $\sigma_k$ | 1.0 | 1.0 | 1.0 |
| $\sigma_\varepsilon$ | 1.3 | 1.3 | 1.3 |
| $C_L$ | 0.25 | 0.23 | 0.23 |
| $C_\eta$ | 85 | 70 | 70 |

Table 2.1: $\overline{v^2} - f$ model constants

## Comparison of the Three $\overline{v^2} - f$ Models in Fully Developed Channel Flow

The analytical comparison of the farfield behavior in the previous section only give an indication of what to expect from the models in a limited region of the flow. Of greater interest is how the models perform in the simple test case of fully developed channel flow (1D) that allows for comparison all the way through the boundary layer, which indeed is the region where we expect to benefit the most from solving the two additional partial differential equations compared to two-equation turbulence models.

From Figure 2.2(b) we see that all three models give about the same estimates for the shear stress component, $\overline{uv}$, which is the only Reynolds stress of importance as far as the mean flow is concerned. The results are close to that of DNS but the slight undershoot at $y^+$ values around 50 is enough to overpredict the mean velocity, shown in Figure 2.2(a) by some 10% in a large part of the channel. Obviously, from Figure 2.2(c), it is the too low values of $\nu_t$ at $50 < y^+ < 100$ that cause the $\overline{uv}$ undershoot. Away from the wall the high values of $\nu_t$ are balanced by the low gradient in this region giving a very accurate estimate of $\overline{uv}$. In Figures 2.2(d)-2.2(f) the variables used to calculate $\nu_t$ are plotted and it is clear that the $\overline{v^2}$ distribution is the main source of error in the $\nu_t$ expression. It is also in the $\overline{v^2}$ profiles the models differ the most. For example, in the freestream region Model 3 overpredict the level of $\overline{v^2}$ by almost 80%, whereas Model 1 is much closer to the DNS profile (30% above).
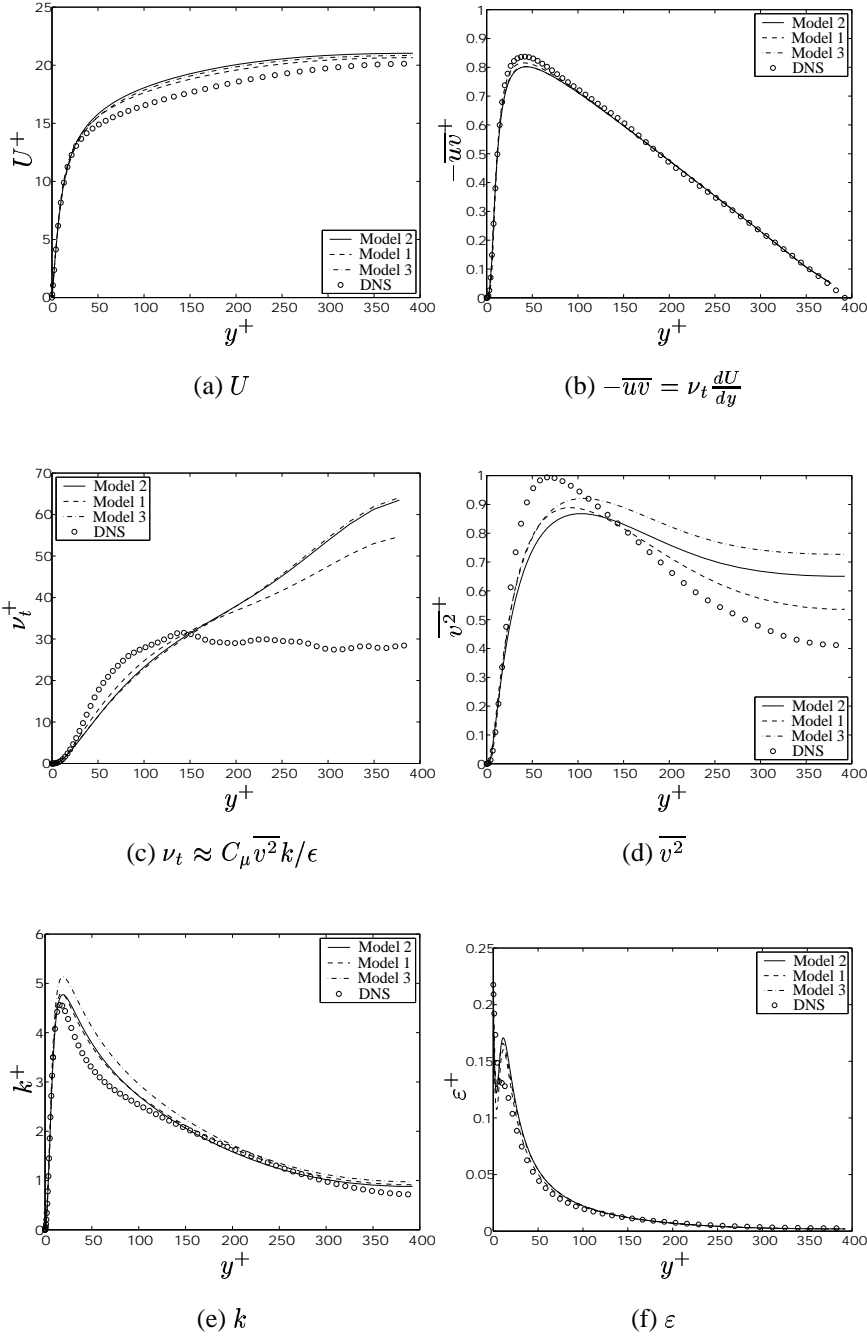
25

(a) $U$

(b) $-\overline{uv} = \nu_t \frac{dU}{dy}$

(c) $\nu_t \approx C_\mu v^2 k/\epsilon$

(d) $\overline{v^2}$

(e) $k$

(f) $\varepsilon$

Figure 2.2: Various results from channel flow computations

26

## 2.3.4 Wall Boundary Conditions for some Turbulent Quantities

In this section the wall boundary conditions for the modelled dissipation rate, $\varepsilon$, and the relaxation parameter, $f$, are derived. For a review on near-wall turbulence modelling including analysis of near-wall behaviour of turbulent quantities consult Patel *et al.* (1985).

**The $\varepsilon$ wall boundary condition**

The boundary value of turbulent kinetic energy on a solid wall is identically zero due to the no-slip concept. In order to obtain the boundary condition for the dissipation rate of turbulent kinetic energy expand the fluctuating velocities according to

$$
\begin{aligned}
u &= a_0 + a_1 y + a_2 y^2 \ldots \\
v &= b_0 + b_1 y + b_2 y^2 \ldots \\
w &= c_0 + c_1 y + c_2 y^2 \ldots
\end{aligned}
\tag{2.50}
$$

The coefficients can be functions of anything but $y$ and are zero if averaged. The no-slip condition gives $a_0 = b_0 = c_0 = 0$. Continuity and the fact that $(\partial u/\partial x)_{y=0} = (\partial w/\partial z)_{y=0} = 0$ (no-slip) gives $(\partial v/\partial y)_{y=0} = 0$. Therefore $b_1$ too must be equal to zero and the behavior of the wall normal and tangential Reynolds stresses are found by squaring and averaging the expressions for the fluctuating velocities. The sum of these three stresses gives twice the turbulent kinetic energy.

$$
\begin{aligned}
\overline{u^2} &= \overline{a_1^2} y^2 + \mathcal{O}(y^3) \\
\overline{v^2} &= \overline{b_2^2} y^4 + \mathcal{O}(y^5) \\
\overline{w^2} &= \overline{c_1^2} y^2 + \mathcal{O}(y^3) \\
k &= \frac{1}{2}(\overline{a_1^2} + \overline{c_1^2}) y^2 + \mathcal{O}(y^3)
\end{aligned}
\tag{2.51}
$$

The modelled (homogeneous) dissipation rate is defined in Eqn. 2.52. We will now show that we can express the near wall dissipation rate in terms of the kinetic energy itself and use this relation as boundary condition for $\varepsilon$.

$$
\varepsilon \equiv \nu \overline{\frac{\partial u_j}{\partial x_i} \frac{\partial u_j}{\partial x_i}}
\tag{2.52}
$$

27

In the vicinity of walls all $\partial/\partial x$ and $\partial/\partial z$ terms are negligible compared to the $\partial/\partial y$ terms and we can use the Taylor expansions for the fluctuating velocities in Eqn. 2.50 to estimate the dissipation rate near walls. We get

$$\begin{aligned} \varepsilon &\approx \nu \overline{\left( \left( \frac{\partial u}{\partial y} \right)^2 + \left( \frac{\partial w}{\partial y} \right)^2 \right)} \\ &= \nu \left( \overline{a_1^2} + \overline{c_1^2} \right) + \mathcal{O}(y) \end{aligned} \tag{2.53}$$

The same quantity as for the kinetic energy (Eqn. 2.51), $\overline{a_1^2} + \overline{c_1^2}$, appears allowing to express the near wall behavior of $\varepsilon$ in terms of $k$ according to

$$\varepsilon \to 2\nu \frac{k}{y^2} \quad \text{as} \quad y \to 0 \tag{2.54}$$

Hence, the two wall boundary conditions used are $k = 0$ and that $\varepsilon/\nu$ and $2k/y^2$ must have the same limit as walls are approached. By forcing $\varepsilon$ to take this value at the first interior computational node the correct limit is enforced.

Note that in this derivation we have assumed that the higher order terms in the Taylor expansion of $\varepsilon$ can be neglected compared to the zero order term $\varepsilon_{wall}$, i.e. that $\varepsilon$ really is constant for $y^+$ values lower than the $y^+$ value of the first node, which typically is of order 1. In Figure 2.3 the $\varepsilon$ profiles from DNS data and the three $\overline{v^2} - f$ models are plotted for $0 < y^+ < 5$. Clearly, the assumption of $\varepsilon$ being constant at $y^+ \approx 1$ can be questioned. Indeed, if $\varepsilon$ really was approaching a constant value it should not matter whether this value is used *on* the boundary or at the first interior node. In this case of approximately constant $\varepsilon$ the natural boundary condition to set would be $\partial \varepsilon/\partial y = 0$.

### The $f$ Boundary Condition

In Section 2.3.3 the $f$ wall boundary condition for Model 1 was derived from the definition of the $\overline{v^2}$ equation source term, $kf$. The approach originally suggested was to force the correct behaviour of $\overline{v^2}$, i.e. $\overline{v^2} = \mathcal{O}(y^4)$ (cf. Eqn. 2.51), close to walls using the wall value of $f$ in a way similar to how the $\varepsilon$ wall value was set to give the correct near-wall asymptote of $\varepsilon$.

The no-slip boundary condition for wall normal Reynolds stress is $\overline{v^2} = 0$. To get a wall boundary condition for $f$ we must study the $\overline{v^2}$ equation, which at small distance away from walls reads

$$\nu \frac{\partial^2 \overline{v^2}}{\partial y^2} - \overline{v^2} \frac{\varepsilon}{k} + kf = 0 \tag{2.55}$$
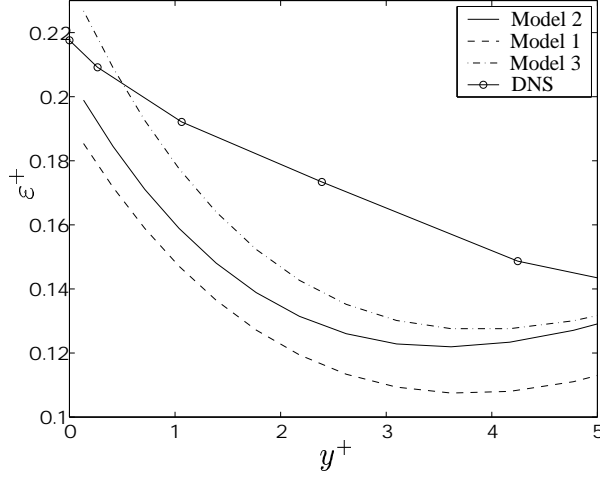
28

PSfrag replacements

Figure 2.3: Near-wall dissipation rate for DNS and $\overline{v^2} - f$ Models 1–3

In this equation $k$ is replaced using Eqn. 2.54 (assuming it is valid) and the equation can be written as

$$\frac{\partial^2 \overline{v^2}}{\partial y^2} - 2\frac{\overline{v^2}}{y^2} + \frac{\varepsilon f}{2\nu^2}y^2 = 0 \qquad (2.56)$$

Close to walls (very close) $f$ and $\varepsilon$ are constant with respect to $y$ and the ordinary differential equation can be solved. The solution is

$$\overline{v^2} = Ay^2 + \frac{B}{y} - \varepsilon f\frac{y^4}{20\nu^2} \qquad (2.57)$$

and for $\overline{v^2}$ to behave as $\mathcal{O}(y^4)$ the integration constants $A$ and $B$ must be equal to zero. Hence, the boundary condition for $f$ is

$$f = -\frac{20\nu^2}{\varepsilon}\frac{\overline{v^2}}{y^4} \qquad (2.58)$$

## 2.4   Realizability

A common deficiency of eddy viscosity based turbulence models is that they overpredict the turbulent kinetic energy (TKE) in stagnation point flows. Durbin (1995$a$) suggested the use of a "realizability" constraint, $2k \geq \overline{u^2} \geq 0$, in

29

order to limit the growth of TKE in regions where standard eddy-viscosity based expressions for the Reynolds stresses take erroneous values. Durbin expressed this constraint in terms of a limit on the turbulent time scale, $\mathcal{T}$, which greatly improves TKE predictions. This approach is discussed in detail below.

### 2.4.1 Derivation of the Time Scale Constraint

All eddy-viscosity based turbulence models use the following expression when calculating the Reynolds stresses appearing in the RANS equations

$$\overline{u_i u_j} = -2\nu_t S_{ij} + \frac{2}{3}k\delta_{ij} \tag{2.59}$$

It is well known that this model gives abnormal levels of TKE in stagnation regions. This problem can be dealt with in several ways of which the (Kato & Launder (1993)) "$S_{ij}\Omega_{ij}$" and the Durbin (1995$a$) time scale approaches are the most commonly used. In the former $S_{ij}S_{ij}$ in the modelled production, $P_k$ (cf. Eqn. 2.16), is replaced by $S_{ij}\Omega_{ij}$. This modification improves the prediction of $k$ in stagnation regions but is wrong in principle (it is within the model of $\nu_t$ the error lies). As will be shown below the latter approach does not require any physically questionable changes of the turbulence model.

Durbin showed that the constraints $2k \geq \overline{u^2} \geq 0$, of which the latter is the most stringent, can be used to derive a bound on the turbulent time scale $\mathcal{T}$ (e.g. $k/\varepsilon$ in $k$-$\varepsilon$ models). This constraint is imposed by finding the eigenvectors of $S_{ij}$, i.e. rotating the coordinate system so that the strain rate tensor $S_{ij}$ becomes diagonal with eigenvalues $\lambda_\alpha$, $\alpha = 1, \ldots, 3$. In this worst case coordinate system (our constraint $\overline{u^2} \geq 0$ must be fulfilled in any coordinate system) all strains are normal and Equation 2.59 can be written as

$$\overline{u_\alpha^2} = -2\nu_t\lambda_\alpha + \frac{2}{3}k \tag{2.60}$$

Imposing our constraint $\overline{u^2} \geq 0$ gives

$$2\nu_t\lambda_\alpha \leq \frac{2}{3}k \tag{2.61}$$

Solving the characteristic equation for $\lambda_\alpha$ we have that $|\lambda_\alpha| = \sqrt{|S|^2/2}$ in two dimensions and that

$$|\lambda_\alpha| \leq \sqrt{2|S|^2/3} \tag{2.62}$$

30

in three dimensions. Equations 2.61 and 2.62 may now be used to obtain a lower limit on $\nu_t$

$$\nu_t \leq \frac{k}{3 \max \lambda_\alpha} \tag{2.63}$$

Now insert Equation 2.11 for $\nu_t$ to obtain

$$C_\mu \mathcal{V}^2 \mathcal{T} \leq \frac{k}{3 \max \lambda_\alpha} \tag{2.64}$$

Division by $C_\mu \mathcal{V}^2$ gives the constraint Durbin uses, i.e.

$$\mathcal{T} \leq \frac{k}{3 C_\mu \mathcal{V}^2} \frac{1}{\max \lambda_\alpha} \tag{2.65}$$

For $k$-$\varepsilon$ models this implies

$$\mathcal{T} = \min \left( \frac{k}{\varepsilon}, \frac{1}{3 C_\mu} \frac{1}{\max \lambda_\alpha} \right) \tag{2.66}$$

whereas for $\overline{v^2}$-$f$ models

$$\mathcal{T} = \min \left( \max \left( \frac{k}{\varepsilon}, 6 \sqrt{\frac{\nu}{\varepsilon}} \right), \frac{k}{3 C_\mu \overline{v^2}} \frac{1}{\max \lambda_\alpha} \right) \tag{2.67}$$

and for $k$-$\omega$ models

$$\mathcal{T} = \min \left( \frac{1}{\omega}, \frac{1}{3 \gamma^* \max \lambda_\alpha} \right) \tag{2.68}$$

The above idea originates from investigating the turbulent time scale near stagnation points where it is argued that $\mathcal{T}$ becomes very large. The too high values of $\mathcal{T}$ lead to an underestimation of the modelled production of dissipation rate in the $\varepsilon$ equation. The consequence will be a too low estimate of $\varepsilon$ that explains the high levels of TKE. However, this argument seems to be wrong, which can be seen by a closer look at the source terms in the $\varepsilon$ equation that read

$$\frac{C_{\varepsilon 1} 2 \nu_t S_{ij} S_{ij} - C_{\varepsilon 2} \varepsilon}{\mathcal{T}}, \tag{2.69}$$

31

or

$$2C_{\varepsilon 1}C_\mu \overline{v^2} S_{ij}S_{ij} - \frac{C_{\varepsilon 2}\varepsilon}{\mathcal{T}} \tag{2.70}$$

where Eqn. 2.16 and 2.11 has been used to replace the TKE production term $P_k$ in the $\varepsilon$ equation.

Now it is obvious that the effect a limitation of the time scale has in the $\varepsilon$ equation is not to increase the production of $\varepsilon$ but to increase its dissipation. The increase in dissipation of $\varepsilon$ will lower the level of $\varepsilon$, i.e. decrease the dissipation rate of TKE, and lead to *higher* levels of TKE. As the time scale bound was introduced in order to decrease the TKE the effect of limiting $\mathcal{T}$ in the $\varepsilon$ equation cannot be the reason why the time scale bound idea works so well.

The reason why the realizability constraint works is the effect of the time scale limitation in the expression for the turbulent viscosity, Equation 2.11. This relation used in the formula for production of TKE gives

$$P_k = 2C_\mu \overline{v^2} \mathcal{T} S_{ij}S_{ij} \tag{2.71}$$

Obviously a decrease in $\mathcal{T}$ will also decrease the production rate of $k$. Hence, this must be the explanation of the improvement in the predictions of the turbulent kinetic energy levels.

## 2.4.2 On the Use of Realizability Constraints in the $\overline{v^2}$-$f$ Model

This discussion on the realizability constraint will be based on the $\overline{v^2} - f$ turbulence model by Lien & Kalitzin (2001) (Model 2). They use the same constraint on the turbulent time scale as was originally suggested by Durbin with the addition of a model constant, hereafter referred to as $C_{lim}$ set to 0.6, leading to

$$\mathcal{T} = \min\left[\max\left[\frac{k}{\varepsilon}, 6\sqrt{\frac{\nu}{\varepsilon}}\right], \frac{C_{lim}k}{\sqrt{6}C_\mu \overline{v^2}S}\right] \tag{2.72}$$

As already discussed in the previous section the use of this realizability limit greatly improves TKE predictions. Below the use of this limit in the $\overline{v^2}$ and $f$ equations (Eqn. 2.43 and 2.44) is investigated.

In order to illustrate the effect of realizability rewrite the $f$ equation 2.44 on standard transport equation form

$$0 = \frac{C_2 P_k}{L^2 k} + \frac{1}{\mathcal{T}L^2}\left[(6 - C_1)\frac{\overline{v^2}}{k} + \frac{2}{3}(C_1 - 1)\right] - \frac{f}{L^2} + \frac{\partial^2 f}{\partial x_j^2} \tag{2.73}$$

32

The first two terms are source terms ($C_1 = 1.4$), the third act as a sink whereas the last term is a diffusive term. Now imagine our time scale limiter being active. This means that $P_k$ in the first source term will decrease as in the $k$ equation (it is not clear whether the quantity $P_k/k$ will actually decrease or increase). This decrease will to some extent be balanced by an increase of the second source term as this term is multiplied by $1/\mathcal{T}$. This counteracting effect is incorrect in principle as $kf$ forms the source term in the $\overline{v^2}$ equation.

Finally, from inspection of Equation 2.72, we have that the possible increase of $\overline{v^2}$ can further reduce the time scale $\mathcal{T}$. This type of positive feedback has caused some of my computations to diverge as $f$ becomes increasingly larger. Recall the $f$ equation is of elliptic nature and that any perturbation is felt in the entire computational domain.

The easiest way to get around this problem is to not use the time scale limit at all in the $f$ equation. Another possible route is to rewrite the realizability constraint in terms of $\overline{v^2}/k$, e.g.

$$\frac{\overline{v^2}}{k} = \min\left[\frac{\overline{v^2}}{k}, \frac{C_{lim}}{\sqrt{6}C_\mu T S}, 2\right] \tag{2.74}$$

Using this limit in the $f$ equation will consistently lower the $\overline{v^2}$ part of the turbulent kinetic energy.

Finally, Lien & Kalitzin (2001) suggested a similar bound on the turbulent length scale $L$, appearing in the $f$ equation only, according to

$$L = C_L \max\left(\min\left(\frac{k^{3/2}}{\varepsilon}, \frac{k^{3/2}}{\sqrt{6}C_\mu \overline{v^2} S}\right), C_\eta \frac{\nu^{3/4}}{\varepsilon^{1/4}}\right) \tag{2.75}$$

Computations of a the flow in a stator vane passage indicates that the level of TKE, once the solution is fully converged, is not very sensitive to how realizability is used in the $\overline{v^2}$ and $f$ equations. These results will be further discussed in later chapters.

**The Consequence of Realizability in the Farfield**

In Section 2.3.3 the farfield limiting behaviour of the $\overline{v^2}$ equation was derived. In that derivation it was assumed that the turbulent time scale $\mathcal{T}$ could be replaced using $\mathcal{T} = k/\varepsilon$. However, if the realizability constraint is active this assumption

is not valid. Rederiving the farfield behaviour of the $\overline{v^2}$ equation source term more carefully, i.e. not making the above assumption, yields (cf. Eqn. 2.43-2.46)

$$-\frac{C_1}{\mathcal{T}}\left(\overline{v^2}-\frac{2}{3}k\right)+\frac{1}{\mathcal{T}}\left(6\overline{v^2}-\frac{2}{3}k\right)+C_2 P_k-6\frac{\overline{v^2}}{k}\varepsilon \qquad (2.76)$$

We see that replacing $\mathcal{T}$ by $k/\varepsilon$ directly gives Equation 2.46. Now imagine we have an isotropic turbulent flow $(\overline{v^2}=2k/3)$, in which the production of turbulent kinetic energy is negligible. We get

$$+\frac{12k}{3\mathcal{T}}-\frac{2k}{3\mathcal{T}}-\frac{12}{3}\varepsilon \qquad (2.77)$$

and if $\mathcal{T}=k/\varepsilon$ the dissipation rate of $\overline{v^2}$ will take its correct isotropic value of $2\varepsilon/3$. But when the flow approaches a stagnation region the value of $\mathcal{T}$ becomes smaller than $k/\varepsilon$ (or $\varepsilon < k/\mathcal{T}$) as the time scale bound is activated. As already mentioned the time scale bound ought to decrease $\overline{v^2}$ but clearly, from Eqn. 2.77, it will cause a physically false production of $\overline{v^2}$. Recall that Lien & Kalitzin (2001) modified the $f$ equation in order to have a stable $f$ wall boundary condition and in order to make the model consistent in the farfield then changed the modelled dissipation rate of $\overline{v^2}$. The problem is that when the realizability constraint is active the $\overline{v^2}$ production in the $f$ equation $(6\overline{v^2}/k\mathcal{T})$ is not consistent with the dissipation in the $\overline{v^2}$ equation $(6\overline{v^2}\varepsilon/k)$. And, as this production increases $\overline{v^2}$, which further restrains the time scale bound we might again have positive feedback leading to numerical problems.

The obvious solution to this anomaly is to not use the realizability constraint in the $f$ equation or to change the modelled $\overline{v^2}$ dissipation rate from

$$-6\frac{\overline{v^2}}{k}\varepsilon \quad \text{to} \quad -6\frac{\overline{v^2}}{\mathcal{T}}$$

One of these modification proved to be necessary in order to achieve a converged solution for the stator vane computations where the stagnation region indeed is very large.

# Chapter 3

# Numerical Method

## 3.1  The Solver CALC-BFC

CALC-BFC (Boundary Fitted Coordinates) by Davidson & Farhanieh (1995) is a CFD code for structured meshes based on the finite volume discretization technique described in e.g. Versteeg & Malalasekera (1995). The main features of the code are the use of curvilinear coordinates, the pressure correction scheme SIMPLEC and a co-located grid arrangement with Rhie and Chow interpolation. The equation system solver is a segregated Tri-Diagonal Matrix Solver (TDMA). For a more detailed description see Nilsson (2002), who added multi-block facilities to allow for large, parallel computations in complex domains. The exchange of information among the processors is handled using the Message Passage Interface, MPI.

   For most of the computations the van Leer scheme, which is regarded to be second order accurate, was used when discretizising the momentum equations. The equations governing the turbulence were discretizised with the hybrid scheme, which is first order accurate. Due to convergence problems false time-stepping was used to enhance the numerical stability. A typical calculation of the flow around a stator vane using about 500,000 computational points requires about 40 CPU hours on a Cray Origin 2000.

## 3.2  Description of the Numerical Domain

The structured computational mesh was created using the pre-processor ICEM. This mesh generator is well suited for creating complex structured grids as the
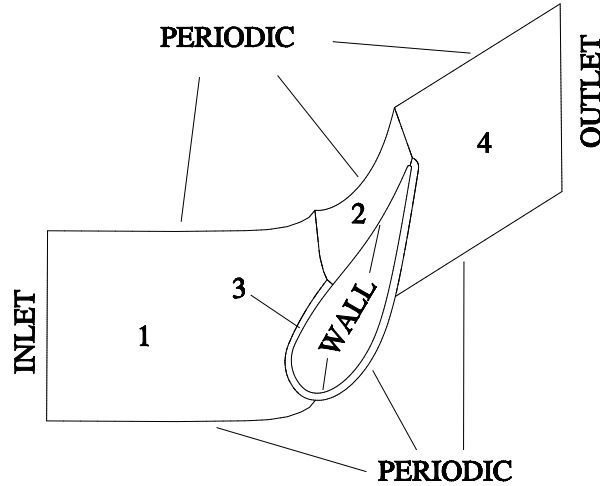
Figure 3.1: The computational domain with boundary conditions and block structure. The blocks are numbered from 1 to 4.

domain can be split into several subdomains in a top-down approach allowing for good control of each subdomain of the mesh. When the mesh is complete the subdomains can be clustered in lager blocks for output.

In most of the simulations the computational domain is a four block domain shown in Figure 3.1. It consists of an O-grid around the stator vane, ensuring high quality cells in the important near-wall region, onto which additional cells were added so that one period of an infinite row of stator vane could be modelled (a part of the O-grid is included in block 2). As the experiment did only consist of two vane passages (cf. Figure 1.4) the assumption of the flow in the measurements being periodic can be questioned. It seems, however, from measured velocities that sufficiently good periodicity is achieved (Radomsky & Thole, 2000*b*).

Also shown are the boundary conditions. The inlet of the domain is located one chord length upstream the stator vane stagnation point. This distance has been used be other investigators (Radomsky & Thole, 2000*b*) and whether it is sufficient or not is discussed in Chapter 4. Finally, as the geometry is symmetric, only one half of the vane passage is analysed and a symmetry boundary condition is applied at the vane midspan.

In Figure 3.2 some regions of the grid are shown in detail. It can be seen that use of the O-grid around the vane gives high quality cells close to the vane but at block-to-block interfaces at various locations around the O-grid there are some abrupt changes in e.g. cell size. This problem could in part have been solved by
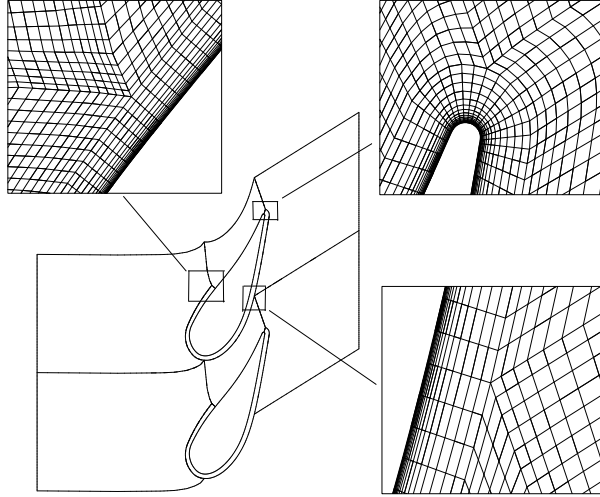
Figure 3.2: Some details of the computational grid

adding an additional O-grid around the present one. Then the additional outer O-grid could have been stretched to fit the geometry between the two blades, whereas the inner O-grid would handle the near-wall stretching. Using this approach the poor cell regions seen in Figure 3.2 could have been moved further out in the freestream, where gradients in general are lower.

## 3.3  Boundary Conditions

### 3.3.1  Inlet

The possibly most uncertain boundary conditions to pose in a RANS simulation is the inlet values of modelled turbulent quantities like the turbulent kinetic energy, $k$, and its dissipation rate, $\varepsilon$. Ideally, all inlet values should be obtained in experiments in order to set up a numerical problem that is as close to reality as possible. The problem is that in many experimental investigations, like the one used to validate the $\overline{v^2} - f$ model in this work, only some of the needed inlet profiles are available. For example, $\varepsilon$ is very difficult to measure at all and is usually obtained via empirical relations to the turbulent length scale.

In this work another approach was used. As the flow entering the vane passage region has developed along a rather long splitter plate it was assumed that the turbulence could be described accurately enough with the equations for fully

developed channel flow. This allows for solving one-dimensional equations for the turbulent quantities using the measured inlet velocity profile as input. These equations read

$$
\begin{aligned}
0 &= \frac{\partial}{\partial y}\left(\left(\nu + \frac{\nu_t}{\sigma_k}\right)\frac{\partial k}{\partial y}\right) + P_k - \varepsilon \\
0 &= \frac{\partial}{\partial y}\left(\left(\nu + \frac{\nu_t}{\sigma_\varepsilon}\right)\frac{\partial \varepsilon}{\partial y}\right) + \frac{C_{\varepsilon 1}P_k - C_{\varepsilon 2}\varepsilon}{\mathcal{T}} \\
0 &= \frac{\partial}{\partial y}\left(\left(\nu + \frac{\nu_t}{\sigma_k}\right)\frac{\partial \overline{v^2}}{\partial y}\right) + kf - \frac{\overline{v^2}}{k}\varepsilon \\
L^2\frac{\partial^2 f}{\partial y^2} - f &= \frac{C_1}{\mathcal{T}}\left(\frac{\overline{v^2}}{k} - \frac{2}{3}\right) - C_2\frac{P_k}{k} - \frac{1}{\mathcal{T}}\left(\frac{\overline{v^2}}{k} - \frac{2}{3}\right)
\end{aligned}
\tag{3.1}
$$

where the dependence on the mean flow enters in the production term, $P_k$ (cf. Eqn. 2.16).

The validity of this method can be questioned as the inlet velocity profile is not fully developed. However, no other, more reliable, way to provide the necessary inlet boundary conditions was found. The measured $U$ profile and the generated $k$ and $\overline{v^2}$ profiles are shown in Figure 3.3. It should be mentioned that the measured velocity profile is very different from fully developed channel flow but also quite different from standard zero pressure gradient boundary layer profiles (Kang *et al.* (1999) explained this with the presence of an adverse pressure gradient in diffuser section of the wind tunnel). The mismatch between the measured and the fully developed velocity profile is responsible for the high levels of $k$ in the boundary layer ($sqrtk/u_* \approx 10$). Note that the inlet boundary condition for $f$ is $\partial f/\partial n = 0$, where $n$ is the normal unit vector of the inlet surface. Hence, no information of $f$ is needed at the inlet.

### 3.3.2   Other

The other types of boundaries conditions in Figure 3.1 are straightforward. The Neumann condition was used for all variables at the outlet. The wall boundary conditions were already discussed in Section 2.3.4 and the periodic condition needs no further explanation.
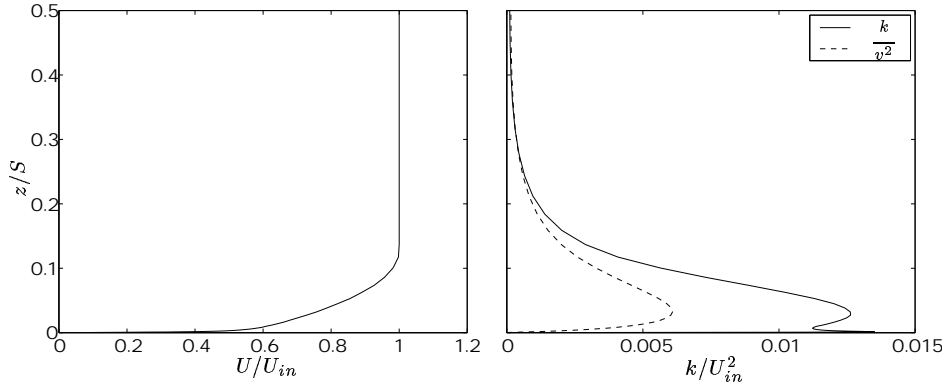
Figure 3.3: The profiles of $U$, $k$ and $\overline{v^2}$ used as inlet boundary conditions. $u_*/U_{in} \approx 0.035$.

## 3.4 Tri-Diagonal Matrix (TDMA) Solvers

As mentioned early in this section CALC-BFC uses a TDMA solver to iteratively solve the matrix equations that result from the discretization procedure. The standard CALC-BFC solver is of segregated nature but as it proved to be necessary to allow for coupled variable treatment at solid boundaries a new coupled TDMA solver was written. In this section both the segregated and the coupled solvers are described.

### 3.4.1 Segregated TDMA Solver

The structure of a tri-diagonal system of equations is given in Eqn 3.2.

$$
\begin{bmatrix}
D_2 & -A_2 & 0 & \dots & & \\
-B_3 & D_3 & -A_3 & 0 & \dots & \\
0 & -B_4 & D_4 & -A_4 & 0 & \dots \\
\vdots & \ddots & \ddots & \ddots & \ddots & \ddots
\end{bmatrix}
\begin{bmatrix}
\phi_2 \\
\phi_3 \\
\phi_4 \\
\vdots
\end{bmatrix}
=
\begin{bmatrix}
C_2 + B_2\phi_1 \\
C_3 \\
C_4 \\
\vdots
\end{bmatrix}
\tag{3.2}
$$

A TDMA solver is based on Gauss-Elimination. The first step is to get rid of the left diagonal in the matrix, i.e. all the B's, which means that the right diagonal and the load vector coefficients are modified according to Eqn. 3.3 and 3.4 starting with the top row and then working through the matrix.

39

$$
\begin{aligned}
A_2^{mod} &= D_2^{-1} A_2 \\
C_2^{mod} &= D_2^{-1} \left[ C_2 + B_2 \phi_1 \right]
\end{aligned}
\tag{3.3}
$$

$$
\begin{aligned}
A_i^{mod} &= \left[ D_i - B_i A_{i-1}^{mod} \right]^{-1} A_i \qquad i = 3, 4 \ldots i_{max} - 1 \\
C_i^{mod} &= \left[ D_i - B_i A_{i-1}^{mod} \right]^{-1} \left[ C_i + B_i C_{i-1}^{mod} \right]
\end{aligned}
\tag{3.4}
$$

After this operation the unknowns can be determined by recursive use of the equation

$$
\phi_i = C_i^{mod} + A_i^{mod} \phi_{i+1}
\tag{3.5}
$$

### 3.4.2 Coupled TDMA Solver

In order to enhance numerical stability it is sometimes beneficial to solve coupled equations. The coupled equations approach enables implicit formulation of for example boundary conditions where one flow field variable can be expressed in terms of another variable. Look for example at the boundary condition for $f$ in the turbulence model suggested by Durbin (1995$b$)

$$
f_{\text{wall}} = \frac{-20\nu^2}{\varepsilon} \left( \frac{\overline{v^2}}{y^4} \right)_{\text{wall}}
\tag{3.6}
$$

In this expression for the wall value of $f$ we see a coupling with two other flow field variables (if $\nu$ is a constant). When using the standard segregated approach where $\overline{v^2}$ and $\varepsilon$ has been recalculated separately a change in $\overline{v^2}/\varepsilon$ is multiplied by a factor of $-20\nu^2/x_n^4$. In the vicinity of wall boundaries the latter quantity is in my computations of order $10^{13}$ and it is obvious that even a small change in $\overline{v^2}/\varepsilon$ undergoing this strong amplification can lead to oscillations, or worse, divergence in the $f$-equation.

Now imagine that the $\overline{v^2}$ and $f$ sets of equations are combined into one system of equations. This allows to implicitly remove the sensitivity of $f$ at boundaries to changes in $\overline{v^2}$ by adding coefficients in the left hand side matrix. The new larger

matrix is arranged as described in Eqn 3.7 (suggested by Eriksson (2002)) for a TDMA sweep in the $i$-direction without introducing any coupling between $\overline{v^2}$ and $f$ (for definition of coefficients $a_P, a_W, \ldots$ see Versteeg & Malalasekera (1995)).

$$
\begin{bmatrix}
a_{P2_{\overline{v^2}}} & 0 & -a_{E2_{\overline{v^2}}} & 0 & \cdots & & \\
0 & a_{P2_f} & 0 & -a_{E2_f} & 0 & \cdots & \\
-a_{W3_{\overline{v^2}}} & 0 & a_{P3_{\overline{v^2}}} & 0 & -a_{E3_{\overline{v^2}}} & 0 & \cdots \\
0 & -a_{W3_f} & 0 & a_{P3_f} & 0 & -a_{E3_f} \\
\vdots & \ddots & \ddots & \ddots & \ddots & \ddots & \ddots
\end{bmatrix}
\begin{bmatrix}
\overline{v^2}_2 \\
f_2 \\
\overline{v^2}_3 \\
f_3 \\
\vdots
\end{bmatrix}
=
$$

$$
=
\begin{bmatrix}
c_{2_{\overline{v^2}}} + a_{W2_{\overline{v^2}}}\overline{v^2}_{wall} \\
c_{2_f} + a_{W2_f} f_{wall} \\
c_{3_{\overline{v^2}}} \\
c_{3_f} \\
\vdots
\end{bmatrix}
\tag{3.7}
$$

Now the $f$ boundary condition and the source term in the $\overline{v^2}$ equation can be introduced implicitly. For example, if our $i = 1$ boundary is a wall we can implement the boundary condition given by Eqn. 3.6 by adding the coefficient $F_{bc}$ at the matrix position giving the connection of the first interior $f$ value with the $f$ wall value. Implicit treatment of the source term $-kf$ in the $\overline{v^2}$ equation corresponds to adding the coefficient $S_{\overline{v^2}}$. $F_{bc}$ and $S_{\overline{v^2}}$ are given by Eqn. 3.8

$$
\begin{aligned}
F_{bc} &= \frac{20\nu^2}{\varepsilon x_n^4} a_{2W_f} \\
S_{\overline{v^2}} &= -\rho k V
\end{aligned}
\tag{3.8}
$$

$$
\begin{bmatrix}
a_{P2_{\overline{v^2}}} & S_{\overline{v^2}} & -a_{E2_{\overline{v^2}}} & 0 & \cdots & & \\
F_{bc} & a_{P2_f} & 0 & -a_{E2_f} & 0 & \cdots & \\
-a_{W3_{\overline{v^2}}} & 0 & a_{P3_{\overline{v^2}}} & S_{\overline{v^2}} & -a_{E3_{\overline{v^2}}} & 0 & \cdots \\
0 & -a_{W3_f} & 0 & a_{3P_f} & 0 & -a_{E3_f} & \\
\vdots & \ddots & \ddots & \ddots & \ddots & \ddots & \ddots
\end{bmatrix}
\begin{bmatrix}
\overline{v^2}_2 \\
f_2 \\
\overline{v^2}_3 \\
f_3 \\
\vdots
\end{bmatrix}
=
$$

$$
=
\begin{bmatrix}
c_{2_{\overline{v^2}}} + a_{W2_{\overline{v^2}}}\overline{v^2}_{wall} \\
c_{2_f} \\
c_{3_{\overline{v^2}}} \\
c_{3_f} \\
\vdots
\end{bmatrix}
\tag{3.9}
$$

This approach has two main disadvantages. The memory requirement increase as we must be able to handle matrices of size $2i_{max}$ by $2i_{max}$ instead of $i_{max}$ by $i_{max}$. The other drawback is that the matrix now is penta diagonal, which means that it is not possible to use a standard TDMA solver. Not much can be done to deal with the first problem whereas it is fairly easy to rewrite a TDMA solver so that it can handle penta diagonal systems of equations. This is done by changing the *scalar* coefficients in the standard TDMA matrix (Eqn. 3.2) to *two by two matrices* and the unknown variable values and the load vector values to vectors of two elements. In this way we get exactly the same structure of the TDMA matrix and can adopt the same solution methodology as for the scalar (special) case with the only difference that all operations now are matrix or vector operations. This is also the reason why, for example, $D_2/A_2$ in Eqn. 3.3 is written on the more general form $A_2^{-1}D_2$. The arrangement of the coefficients for the new TDMA matrix equation is given in Eqn. 3.10 and 3.11.

$$
\begin{aligned}
D_2 &= \begin{bmatrix} a_{Pi_{\overline{v^2}}} & S_{\overline{v^2}} \\ F_{bc} & a_{Pi_f} \end{bmatrix} \\
D_i &= \begin{bmatrix} a_{Pi_{\overline{v^2}}} & S_{\overline{v^2}} \\ 0 & a_{Pi_f} \end{bmatrix} \\
A_i &= \begin{bmatrix} a_{Ei_{\overline{v^2}}} & 0 \\ 0 & a_{Ei_f} \end{bmatrix} \\
B_i &= \begin{bmatrix} a_{Wi_{\overline{v^2}}} & 0 \\ 0 & a_{Wi_f} \end{bmatrix}
\end{aligned}
\tag{3.10}
$$

$$\phi_i = \left[ \begin{array}{c} \overline{v^2}_i \\ f_i \end{array} \right], \qquad C_i = \left[ \begin{array}{c} c_{i_{\overline{v^2}}} \\ c_{i_f} \end{array} \right] \tag{3.11}$$

## 3.5 Visualizing the Secondary Flow Field

Visualizing the horse shoe vortex system of a vane passage flow is rather difficult because the secondary structures are weak compared to main fluid motion between two vanes. Further, as the pressure differences in a vane passage are large, the standard method of plotting isosurfaces of pressure is out of the question. Therefore several authors have suggested different methods to extract the secondary motion from the full velocity field, of which a few were tried in this project.

**Streamlines**

Releasing streamlines into the flow domain is one of the most common flow visualization tools in fluid dynamics as they are easy to understand and directly indicates in what direction the fluid is going. If the streamlines are carefully released at positions in the flow where some flow quantity suggests the presence of secondary motion streamlines can offer valuable information on how the secondary structures evolve.

**Secondary velocites**

In order to quantitatively compare computations with each other and experiments Kang & Thole (2000) defined secondary velocities according to equations 3.12. By this transformation we get the velocity components normal to the midspan mean flow direction $(V_n, V_z)$. This quantity can be interpreted as a measure of the effect of the endwall on the mean flow field.

$$\begin{aligned}
\phi_{ms} &= \arctan(V_{ms}/U_{ms}) \\
V_s &= U \cos \phi_{ms} + V \sin \phi_{ms} \\
V_n &= -U \sin \phi_{ms} + V \cos \phi_{ms} \\
V_z &= w
\end{aligned} \tag{3.12}$$

**Helicity**

This quantity is defined as the scalar product of the vorticity and the local mean velocity, i.e. it measures the amount of vorticity in the direction of the streamlines of the flow. The definition reads

$$H = \underbrace{\varepsilon_{ijk}\partial_j U_k}_{\omega_i} U_i \qquad (3.13)$$

**2:nd Invariant of the Strain Rate Tensor**

The definition of the second invariant of the strain rate tensor, hereafter referred to as the second invariant, reads

$$Q = -\frac{1}{2}\frac{\partial U_i}{\partial x_j}\frac{\partial U_j}{\partial x_i} \qquad (3.14)$$

This quantity was suggested by Hunt *et al.* (1988), who defined a vortex as a region of positive $Q$. $Q$ represents the local balance between shear strain rate and vorticity magnitude (Jeong & Hussain, 1995).

**Examples**

In Figures 3.4—3.5 some examples of how the horseshoe vortices can be illustrated are shown. In Figure 3.4 streamlines were released from a region of high turbulent kinetic energy, $k$, associated with the roll-up of the stagnation vortex (this region of high $k$ is not plotted here but Figure 4.19(a) show a distinct region with high levels of $k$ that could have been used for this purpose). The streamlines released form the two legs of the vortex system. We also see that (hot) fluid from well above the endwall, streamlines B, is dragged downwards replacing the relatively cool gas in the boundary layer, which increases the heat transfer to the endwall. Also included is the contour of the helicity, $H$, in a plane about halfway through the passage. In this plane we see two regions where $H$ is large. They coincide with the released streamlines and can be used to identify the location of the vortices.

In Figure 3.5(a) isosurfaces of the helicity are shown. This quantity gives quite a few structures in the passage but they are hard to distinguish from each other and the vortex in the stagnation region is not visible. This method also suffer from giving high values of $H$ in boundary layers, which makes it hard to decide whether $H$ origins from a boundary layer or from a vortex. Finally, isosurfaces

44
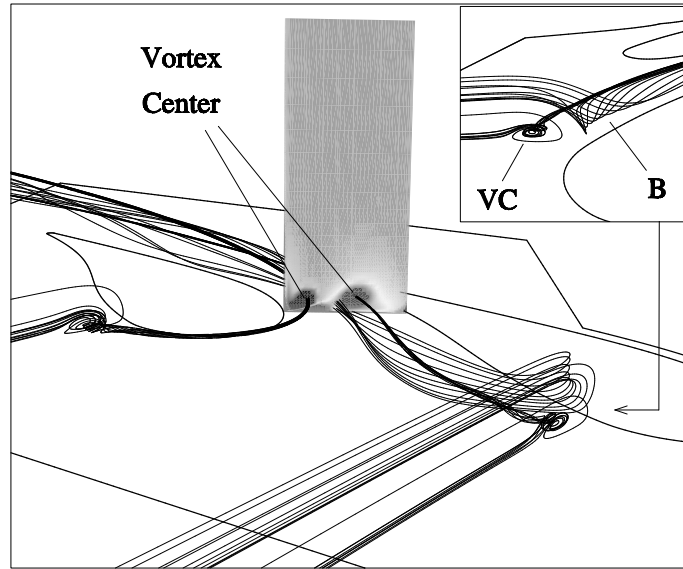
Figure 3.4: Visualization of the two horseshoe vortex legs using streamlines. The plane is plane SS (cf. Figure 4.9) colored by helicity, $H$, indicating the location of the two main vortices.

of the second invariant are shown in Figure 3.5(b). This method is successful in identifying the leading edge vortex but too suffer from giving high values in the boundary layer, in this case almost reproducing the shape of the vanes.
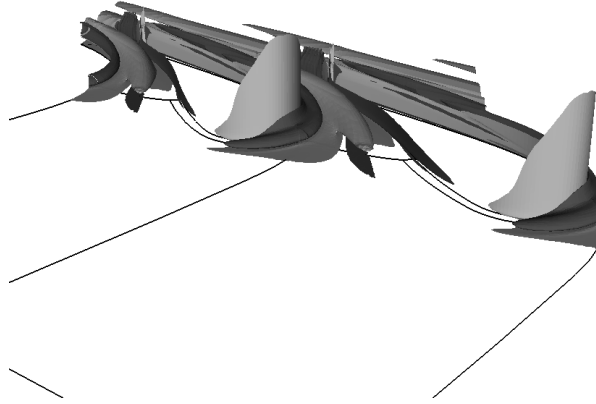
(a) $H$



(b) $Q$
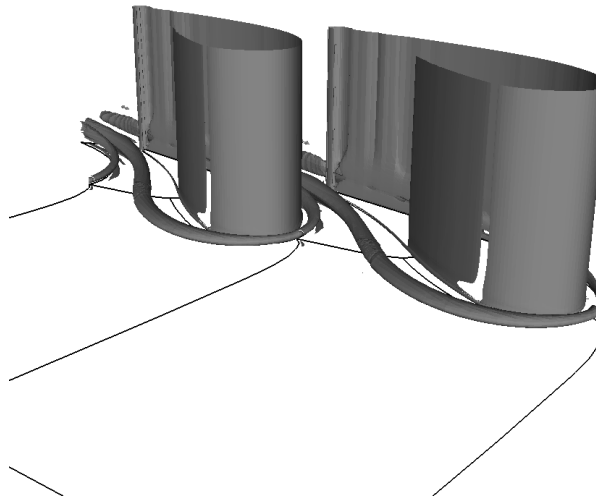
Figure 3.5: Isosufaces of helicity, $H$, and the second invariant of the strain rate tensor, $Q$

# Chapter 4

# Results

## 4.1   Two-dimensional Vane Passage Computations

The flow field in gas turbine vane passages at about half the height (at midspan) of the vane is often assumed to be two-dimensional. This simplification of the real flow substantially reduces the required number of computational points and is used extensively in gas turbine design. In this section the results of some two-dimensional computations of the flow around the stator vane experimentally investigated in Radomsky & Thole (2000$a$) is presented. As this flows has a large stagnation region it is important to investigate the influence and mechanisms of the different types of realizability constraints described in Section 2.4.

### 4.1.1   Static Pressure Coefficient along Vane Midspan

A first indication of the quality of a CFD analysis of any wing profile is the pressure distribution around the profile. One reason for this is that the pressure is not very sensitive to how well boundary layers are resolved as the effect of viscosity becomes small compared to the change in pressure needed to turn (accelerate) the flow along a curved streamline. In fact, solving the Euler equations ($\mu = 0$) is often sufficient in order to get a rather accurate pressure field. Hence, $C_p$ can provide valuable information even if the representation of the effect of turbulence is not accurate.

One important information we get from investigating the near-wall pressure is whether any part of the vane surface contains undesired disturbances, "wiggles". This might very well be the case as the vane surfaces are generated from a set of

47
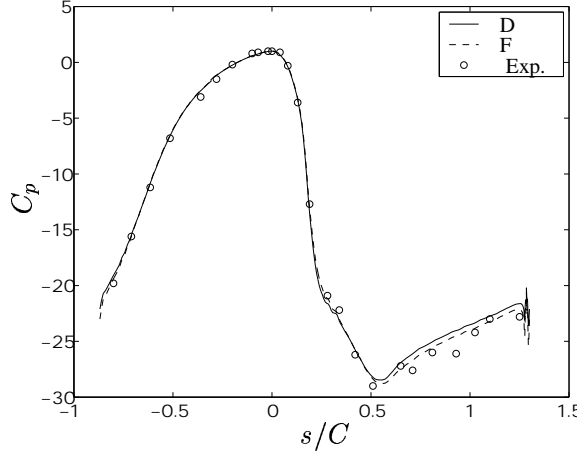
Figure 4.1: Measured and computed static pressure coefficient along stator vane. D: with realizability constraint; F: without.

curves that in turn were created from discrete points measured in the experimental rig in order to have a modelled vane that is as close to the real geometry as possible. The problem lies in converting the discrete set of points into lines of a certain order. If the order of the lines is too low we will have to use a multitude of curves to closely represent the geometry. But if the order is too high the result might be a line lying close to all points but which contain wiggles. The geometry used in this project was built on third or fourth order lines.

In Figure 4.1 the static pressure coefficient, $C_p$, calculated according to

$$C_p = \frac{p_{\text{static}} - p_{\text{static,in}}}{\frac{1}{2}\rho U_{in}^2} \tag{4.1}$$

is plotted for two $\overline{v^2} - f$ computations using Model 1. In order to illustrate $C_p$'s insensitivity to viscosity one case with the realizability constraint active and one case with the constraint turned off were compared. Later in this chapter it will be shown that realizability has a huge impact on the level of turbulent viscosity.

From Figure 4.1 we see that the computed pressure coefficient distribution agrees well with measurements, especially on the pressure side of the vane (for $s/C < 0$), and that there are no disturbances that could have been caused by a poor geometry. In fact, there is a possibility that this was the case in the measurements as there are some irregularities in the experimental data on the suction side. This scatter might be responsible of transition, which later will be shown to occur at about $s/C = 1$.

48
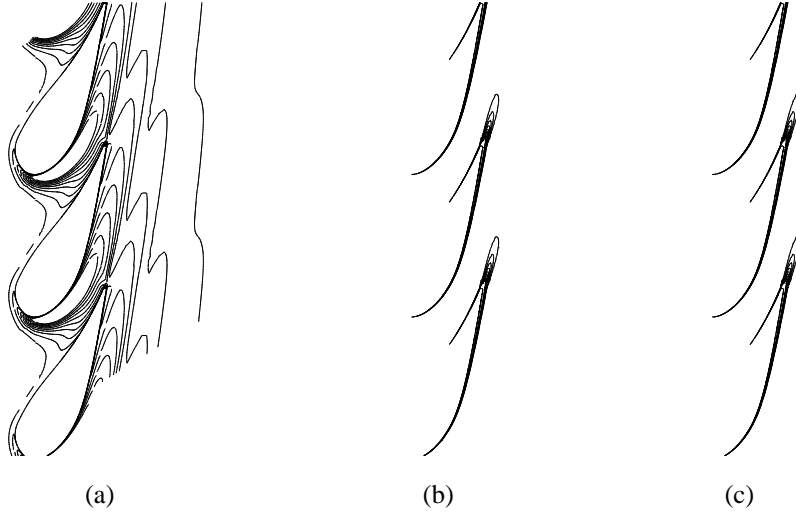
Figure 4.2: Contours of $k/U_{in}^2$. Inlet flow from left. (a) without realizability constraint; (b) with realizability constraint in the $\nu_t$ expression and in the $\varepsilon$ equation. (c) with realizability constraint used everywhere the time scale $\mathcal{T}$ appears. Contour intervals of 0.003, 0.001 and 0.001, respectively.

## 4.1.2 The Effect of the Realizability Constraint in Vane Stagnation Regions

As mentioned in Section 2.4 most eddy-viscosity based turbulence models give unrealistic levels of turbulent kinetic energy in stagnation point flows. In this section the potential of solving this problem using the realizability constraint suggested by Durbin (1995$a$) is investigated. Further, it will be shown that the outstandingly most important effect of the time scale bound is that it prevents the turbulent viscosity $\nu_t$ from taking unphysical values.

In order to illustrate the importance of the realizability constraint the contours of the normalized turbulent kinetic energy ($k/U_{in}^2$) at vane passage midspan are shown in Figure 4.2. In all three cases the same $\overline{v^2} - f$ model, Model 1, has been used with the only difference that in Figure 4.2(a) the realizability constraint, Eqn. 2.67, is deactivated, in Figure 4.2(b) the constraint is used when calculating $\nu_t$ and in the $\varepsilon$ equation, whereas in Figure 4.2(c) it has been used everywhere the time scale $\mathcal{T}$ appears. It can be seen that the constraint has a strong influence on the distribution of $k$. For example, when the limiter is active, it is only in a narrow

49

region close to the wake that $k/U_{in}^2$ exceeds levels of $10^{-3}$, whereas the same quantity is well above this value in almost the entire domain if the constraint is not used. Note that the lowest contour line level in Figure 4.2(a) is 0.003 and 0.001 in Figures 4.2(b) and 4.2(c). Please recall from Section 2.4 that the realizability constraint was written in terms of an upper bound on the turbulent time scale $\mathcal{T}$. As $\mathcal{T}$ appears at several places in the equations governing the $\overline{v^2} - f$ model it would be interesting to find out at which positions a limitation of $\mathcal{T}$ affects the solution. To facilitate the discussion in this section the governing equations are repeated to show exactly where $\mathcal{T}$ appears

$$u_j \frac{\partial k}{\partial x_j} = \frac{\partial}{\partial x_j}\left(\left(\nu + \frac{\nu_t}{\sigma_k}\right)\frac{\partial k}{\partial x_j}\right) + P_k - \varepsilon$$

$$u_j \frac{\partial \varepsilon}{\partial x_j} = \frac{\partial}{\partial x_j}\left(\left(\nu + \frac{\nu_t}{\sigma_\varepsilon}\right)\frac{\partial \varepsilon}{\partial x_j}\right) + \frac{C_{\varepsilon 1} P_k - C_{\varepsilon 2}\varepsilon}{\mathcal{T}}$$

$$u_j \frac{\partial \overline{v^2}}{\partial x_j} = \frac{\partial}{\partial x_j}\left(\left(\nu + \frac{\nu_t}{\sigma_k}\right)\frac{\partial \overline{v^2}}{\partial x_j}\right) + kf - \frac{\overline{v^2}}{k}\varepsilon$$

$$L^2 \frac{\partial^2 f}{\partial x_j^2} - f = \frac{C_1}{\mathcal{T}}\left(\frac{\overline{v^2}}{k} - \frac{2}{3}\right) - C_2 \frac{P_k}{k} - \frac{1}{\mathcal{T}}\left(\frac{\overline{v^2}}{k} - \frac{2}{3}\right)$$

$$\nu_t = C_\mu \overline{v^2} \mathcal{T}$$

$$P_k = \nu_t S_{ij} S_{ij} \qquad (4.2)$$

Clearly, from comparison of Figures 4.2(b) and 4.2(c) showing almost identical results, it must be the use of the time scale bound in the expression for $\nu_t$ that prevents the turbulent kinetic energy from taking erroneous values. From Equations 4.2 we can see that the $k$ equation depends on $\mathcal{T}$ via the production term, $P_k$, which varies linearly with $\mathcal{T}$. Also recall that the only possible effect of the time scale constraint in the $\varepsilon$ equation would be to decrease $\varepsilon$, which increases $k$. Use of the bound also in the $f$ equation seems to have little effect on the solution as Figures 4.2(b) and 4.2(c) are almost identical.

In order to make a quantitative comparison of the effect realizability has on the $k$ distribution $k/U_{in}^2$ is plotted along the midspan stagnation line in Figure 4.3. All these computations are carried out using Model 1. In this investigation several different combinations of the use of realizability in Equations 4.2 were tried. They are all listed in Table 4.1

In Figure 4.3(a) the importance of using the time scale bound when calculating $\nu_t$ is again obvious. The $k$ profile obtained without using the bound has a maximum about 30 times higher than the maximum of any other profile. In order to see

50

| Case | Description |
|------|-------------|
| A | No use of the realizability constraint |
| B | Used everywhere with $C_{lim} = 1.0$ |
| C | In $\nu_t$ expression and $\varepsilon$ equation only |
| D | Same as B but with $C_{lim} = 0.6$ |
| E | Same as D but also in the $\overline{v^2}$ equation where $k/\varepsilon$ has been replaced with $\mathcal{T}$ |
| F | Used everywhere except when calculating $L$ (Eqn. 2.75) |

Table 4.1: Description of how realizability is used when investigating its influence in the stagnation region.



(a) Global view

(b) Close-up
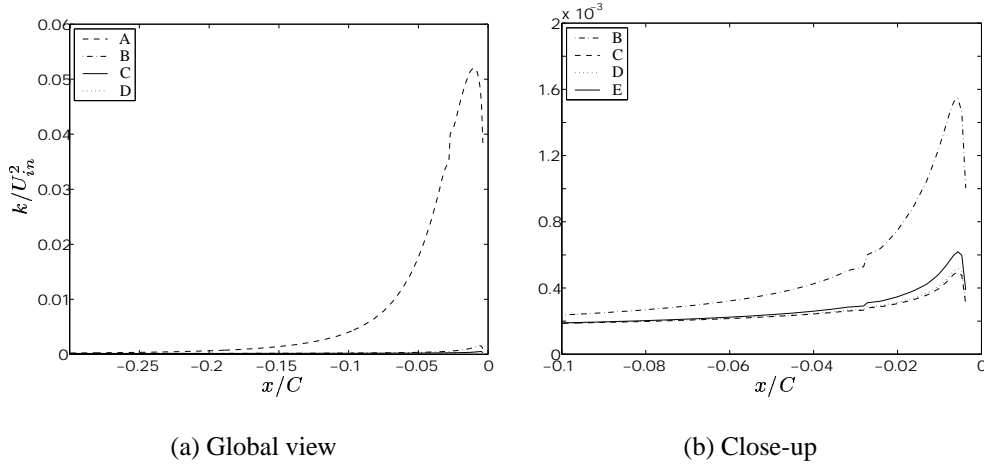
Figure 4.3: Profiles of $k/U_{in}^2$ approaching the midspan vane stagnation point for different realizability constraints. For legend see Table 4.1.
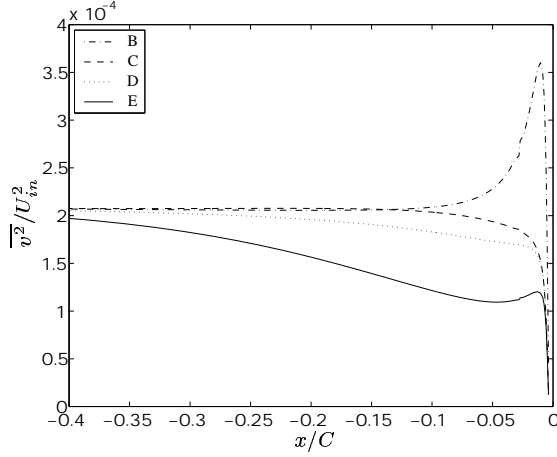
Figure 4.4: Profiles of $\overline{v^2}/U_{in}^2$ approaching the midspan vane stagnation point for different realizability constraints. For legend see Table 4.1.

the differences among the other profiles a close-up is shown in Figure 4.3(b). This figure indicates that if the realizability constraint is to be used the most important parameter, in terms of how $k$ is affected, is the chosen value of the model constant $C_{lim}$. In Section 2.4 it was shown that the physically correct value is 1.0, and that by lowering the value a stronger realizability constraint can be imposed, which allows for model tuning. For the cases C, D and E the results are almost identical. Case F was not included as it gave exactly the same result as case D, which shows that the length scale bound given in Eqn. 2.75 is of minor importance.

For the $\overline{v^2}$ profiles along the stagnation line the differences are somewhat larger. In Figure 4.4 the normalized wall normal Reynolds stress component, $\overline{v^2}/U_{in}^2$, is plotted for Cases B-E (A and F are excluded as A gives very high levels of $\overline{v^2}$ and F the same result as D). We see that for Case B ($C_{lim} = 1.0$) there is still a rather strong peak in the $\overline{v^2}$ profile close to the stagnation point. Unfortunately the experimental set of data needed to verify that this peak indeed is too high is not available.

The other profile that stands out is the E profile. In Case E the ratio $\varepsilon/k$ in the $\overline{v^2}$ equation has been replaced with $\mathcal{T}^{-1}$ as was suggested in Section 2.4.2. The modification was introduced in order to have the correct farfield limiting behaviour in regions where the realizability constraint is active. As can be seen this change decreases the value of $\overline{v^2}$ in almost the entire region upstream the stator vane. Another effect of this change is that close to solid walls the other time scale

52

(a) Global view          (b) Close-up view
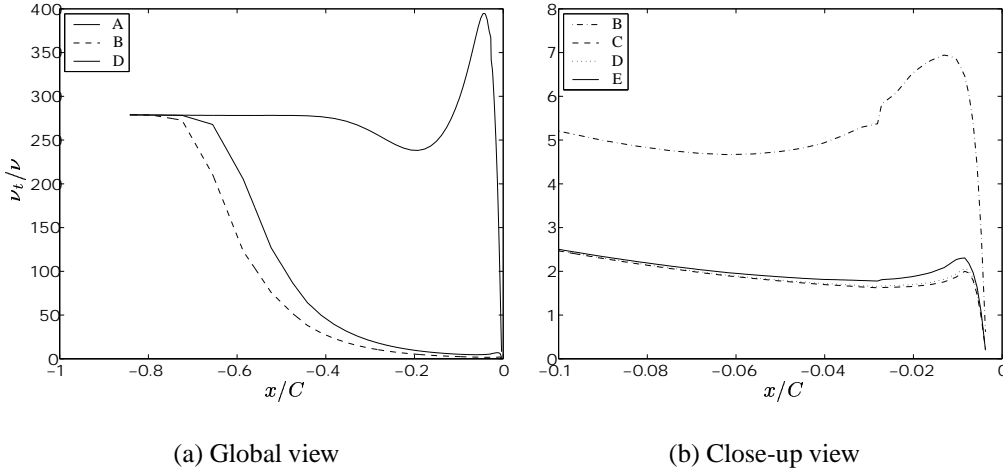
Figure 4.5: Profiles of $\nu_t/\nu$ approaching the midspan vane stagnation point for different realizability constraints. For legend see Table 4.1.

bound expressed in Kolmogorov variables, $\mathcal{T} > 6\sqrt{\nu/\varepsilon}$, modifies the modelled dissipation rate in the $\overline{v^2}$ equation. To be more precise, this makes the $\overline{v^2}$ dissipation rate behave as $y^4$ instead of $y^2$ as $y \rightarrow 0$. This has two implications. Firstly, it will change the near-wall behaviour of $\overline{v^2}$. Secondly, the reduced dissipation rate of $\overline{v^2}$, i.e. an increase in $\overline{v^2}$, seems to improve the numerical stability of the $\overline{v^2} - f$ model.

Finally, the influence of the realizability constraint on the turbulent viscosity, $\nu_t$, is investigated. In Figure 4.5 the profiles of normalized turbulent viscosity $\nu_t/\nu$ along the stagnation line are shown. Just as for the other turbulent quantities the constraint has a remarkable effect on $\nu_t$. As soon as the presence of the vane makes the flow decelerate (or accelerate) the magnitude of the strain rate tensor, $S_{ij}$, becomes large enough to activate the time scale constraint (cf. Eqn. 2.67). And as $\nu_t$ is not governed by a transport equation it immediately reveals where the constraint is activated. From Figure 4.5(b) it can be seen that as long as the constant $C_{lim}$ is the same $\nu_t$ seems to be rather insensitive to whether the time scale bound is used in the $\overline{v^2}$ and $f$ equations or not.

53
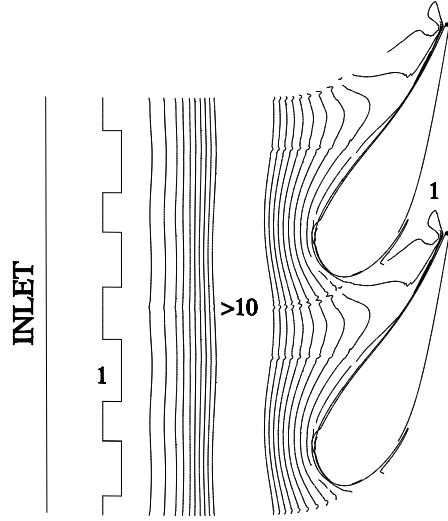
Figure 4.6: Contours of $(k/\varepsilon)/\mathcal{T}$ at midspan indicating in which areas the time scale constraint is active. For values above 1 the constraint is active.

**The Region Where the Time Scale Constraint is Active**

As the realizability constraint has proven to be very important in order to prevent the stagnation point anomaly it is of interest to know where in the domain the constraint is active and how much the time scale, $\mathcal{T}$, is altered. In Figure 4.5(a) we got the indication by studying $\nu_t$ that the limiter is activated almost immediately after the inlet. In Figure 4.6 contours of the ratio $(k/\varepsilon)/\mathcal{T}$ in the symmetry plane are shown. If this ratio is larger than unity the limiter is active and a ratio of 10 means that the standard $\overline{v^2} - f$ time scale, $k/\varepsilon$, has been replaced by a quantity that is 90% smaller.

The strange shape of the first contour just after the inlet is due to the rather coarse mesh in this region. An important observation is that the limiter is activated by the presence of the vane, i.e. the flow must "feel" the vane in order for the limiter to switch on. And as the limiter is active just after the inlet of the computational domain this suggests that the inlet lies too close to stator vane and should be moved perhaps another chord length upstream.

54

### 4.1.3 Boundary Layer Development on a Stator Vane

In order to correctly predict the heat transfer to a gas turbine stator vane it is of crucial importance to have a accurate prediction of how the boundary layer evolves along the vane. This issue is far from straightforward in gas turbine paths as the flow involves, for example, high freestream turbulence, favourable and adverse pressure gradients, possible shock/boundary layer interactions and, perhaps worst of all, transition. Whether the flow is laminar or turbulent will play a significant role when it comes to determining heat transfer. Unfortunately, general multipurpose numerical methods, that could be of practical importance for gas turbine design, of predicting transition still suffer from not being very reliable. For a review of the state of the art of modelling transition consult Savill (2002*a*,*b*).

**The Suction Side**

In Figure 4.7 the boundary layer profiles at five locations of the suction side of the stator vane investigated by Thole *et al.* (2002) are given. Also included are the profiles of a FLUENT $\overline{v^2} - f$ computation. The velocities are scaled with the local freestream velocity, $U_e$, while the wall-normal coordinate $\xi$ is scaled with the local boundary layer thickness, $\delta$. Using this scaling allows to compare the shape of the boundary layers but the comparison is of course only qualitative.

At station SS1, shown in Figure 4.7(b), both the measured and computed profile are laminar. The offset between the two curves can be explained with the uncertainty in estimating the boundary layer thicknesses. At station SS2 the shapes of the profiles are no longer the same. This is due to the transition being predicted too early. At locations SS2 and SS3 the measured profiles are still laminar, whereas the predicted profiles now are fully turbulent. Somewhere in between station SS4 and SS5 transition does occur and the profiles at SS5 match perfectly. As mentioned in Section 4.1.1 and illustrated in Figure 4.1 the experiment show some pressure fluctuations at about the location of lines SS4 (SS4 lies at $s/C = -1.0$). These fluctuations are likely the trace of irregularities in the vane surface and might be responsible for the transition.

Note that these profiles were extracted from a three-dimensional computation, in which a rather course mesh was used (about 500,000 cells), and that the prediction of transition is very sensitive to how well the boundary layer is resolved. Savill (2001) suggests that some 80-100 cells should be used across the boundary layer in order to have a grid independent prediction of transition (the mesh used in this computation has about 20). This fine resolution is not affordable in three-
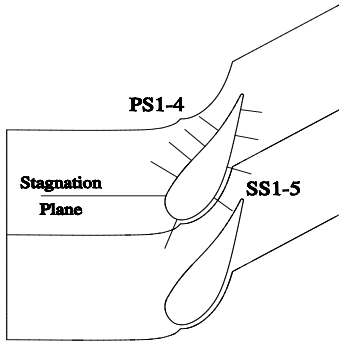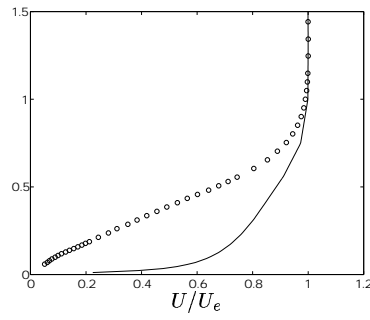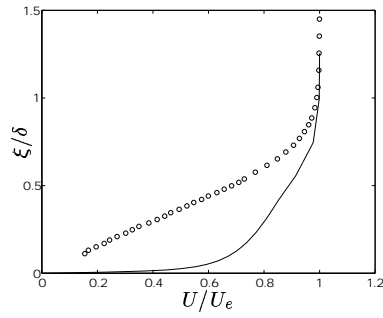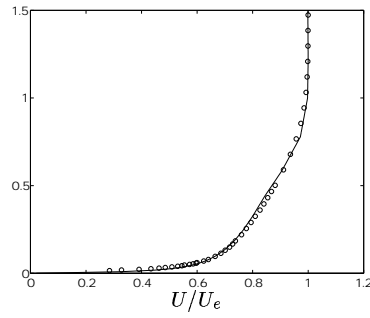
(a) Plotting locations
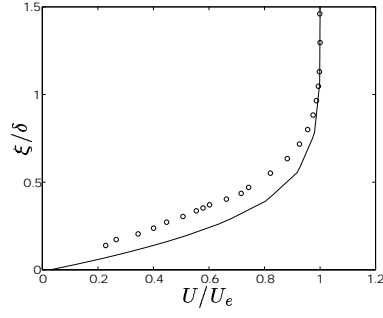
(b) SS1, $s/C = 0.21$
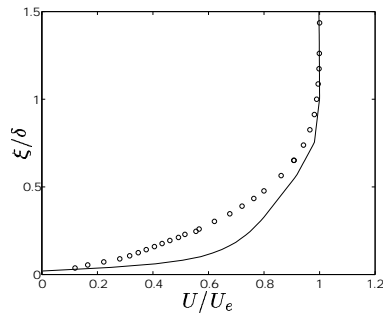
(c) SS2, $s/C = 0.50$

(d) SS3, $s/C = 0.75$

(e) SS4, $s/C = 1.0$

(f) SS5, $s/C = 1.2$

Figure 4.7: Development of the stator vane suction side boundary layer.
○: Experiment; —: FLUENT $\overline{v^2} - f$. $U_e$ denotes the local freestream velocity
and $\xi$ is a wall normal coordinate.

dimensional computations but the grid dependence of transition at midspan could very well have been studied in two dimensions.
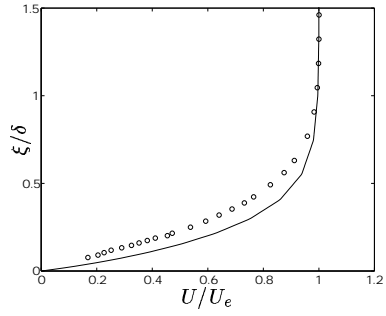
**The Pressure Side**

As for the suction side, the boundary layer development along the pressure side is investigated. In Figure 4.8 the measured and predicted profiles are shown at four pressure side locations. It can be seen that in both experiments and computations the boundary layer remains laminar along the pressure side of the vane due to the stabilizing favourable pressure gradient. This explains the fact that predictions of heat transfer on the pressure side more often agrees with measurements, whereas on the suction side heat transfer is strongly influenced by the predicted location of transition, which, as was illustrated above, is much more difficult.

## 4.2 Three-dimensional Vane Passage Computations

In this section some of the results of the three-dimensional calculations of the flow in a stator vane passage are presented. Focus of the section will be on comparing different turbulence models abilities in predicting the secondary flow structures originating from the junction between the stator vane and its endwall. For this purpose the performance of the turbulence models implemented in the commercial software FLUENT were examined and compared with the predictions of the CALC-BFC $\overline{v^2} - f$ models given in Section 2.3.3.This also allows for comparison of FLUENT and CALC-BFC. A careful investigation of "code-dependence" was conducted by Iaccarino (2001), who implemented the $\overline{v^2} - f$ model in CFX, STAR-CD and FLUENT, via UDF's. Finally, the influence of the realizability constraint on the three-dimensional distributions of turbulent quantities and the mean flow is examined.

All results in this section will be presented as either contour or vector plots in three different planes. Two of them, STAG1 and STAG2, lie in the stagnation plane, whereas the third plane, SS, cuts through the vane passage at about half a chord length into the passage (this plane is defined to be normal to the vane suction surface at a distance $s/C = 0.35$ from the stagnation point, s being a coordinate along the surface of the stator vane). All three planes are shown in Figure 4.9. Included in this figure is the definition of the coordinate $\eta$ associated with plane SS. $\eta$ ranges from 0 to 1, $\eta = 0$ being the suction side and $\eta = 1$ the pressure side.
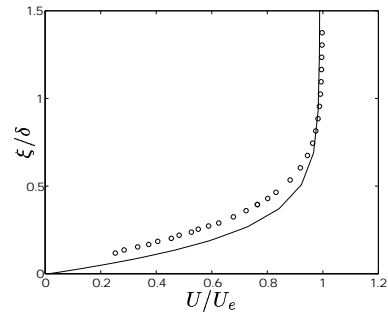
(a) PS1, $s/C = -0.15$
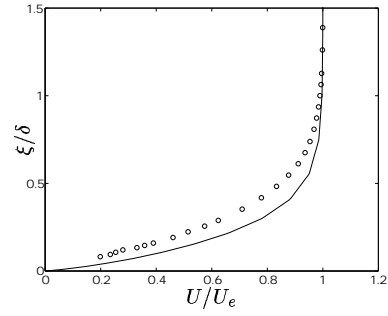
(b) PS2, $s/C = -0.30$
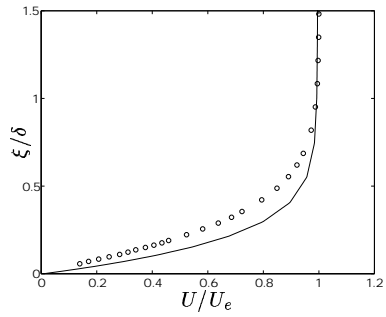
(c) PS3, $s/C = -0.45$

(d) PS4, $s/C = -0.60$

Figure 4.8: Development of the stator vane pressure side boundary layer. ○: Experiment. —: FLUENT $\overline{v^2} - f$. $U_e$ denotes the local freestream velocity and $\xi$ is a wall normal coordinate.
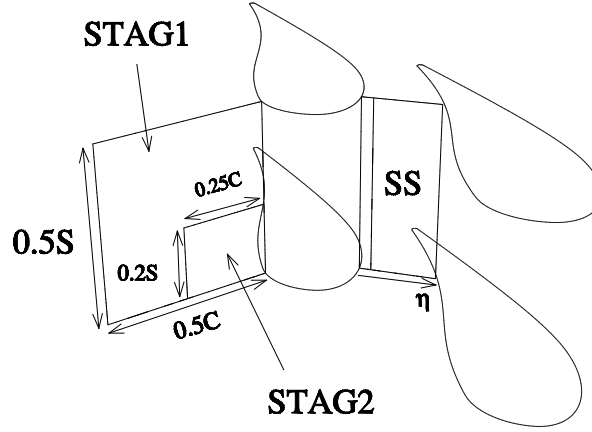
58

Figure 4.9: The different planes used for plotting the results of the three-dimensional computations.

## 4.2.1 Predictions of Secondary Velocities Using FLUENT

In order to visualize the horseshoe vortices emanating from the vane/endwall junction the secondary velocities defined in Section 3.5 (Eqn. 3.12) are plotted in Figure 4.10 for the plane SS. The location of this plane is about halfway through the vane passage (cf. Figure 4.9). As the intensity of the secondary motion is concentrated towards the endwall only one quarter of full passage is included $(0 < z/S < 0.25)$.

From this figure we see that in both the measurements as well as in all computations two secondary structures are present. The structure to the left is the suction side leg of the horseshoe vortex whereas the right structure is the passage vortex (cf. Figure 3.4). The locations of the center of the vortices agree fairly well with the experiment, both lying slightly too close to the stator walls. However, in all computations, especially the Realizable $k - \varepsilon$ one, the strength of the vortices are underpredicted. The model performing the best is the $v^2 - f$ model followed by the RNG $k - \varepsilon$ model. As an indication of how strong the vortex motion is a reference arrow corresponding to a velocity of 5 $m/s$ is included in the top left corner. The maximum total velocity at this location is about $35m/s$.
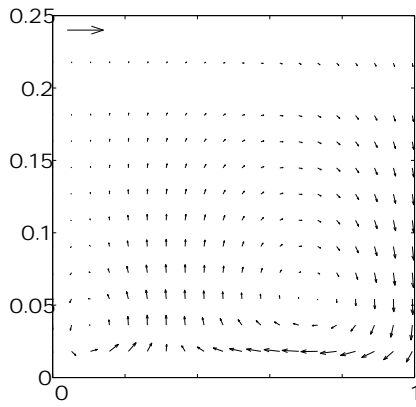
One possible explanation to the inability of reproducing the intensity of the secondary structures could be that the eddy viscosity is overestimated causing the fluid to act too viscously. In that case the vorticity contained in the inlet boundary layer dissipates too rapidly so that its level at plane SS is just a fraction of the
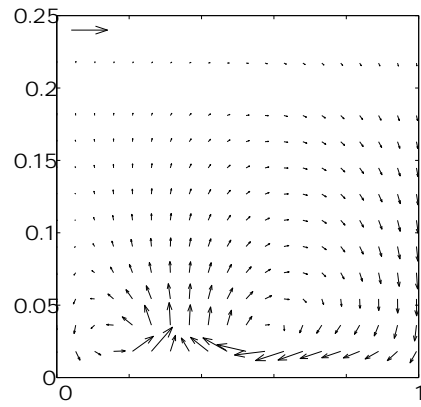
59
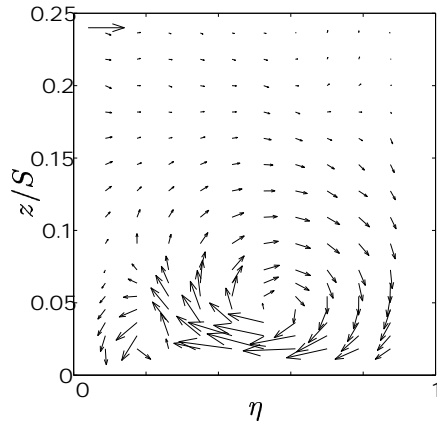
(a) Experiment
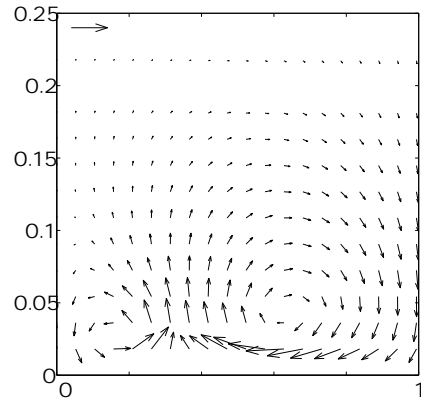
(b) $v^2 - f$

(c) Realizable $k - \epsilon$ (cf. Fig 4.11(c))

(d) RNG $k - \epsilon$

Figure 4.10: Measured and calculated (using FLUENT) secondary velocities in the lower half of plane SS (cf. Figure 4.9). Endwall located at $z = 0$. Suction and pressure surfaces located at $\eta = 0$ and $\eta = 1$, respectively. The arrow in the upper left corner corresponds to $\frac{5}{35}U_\infty$.
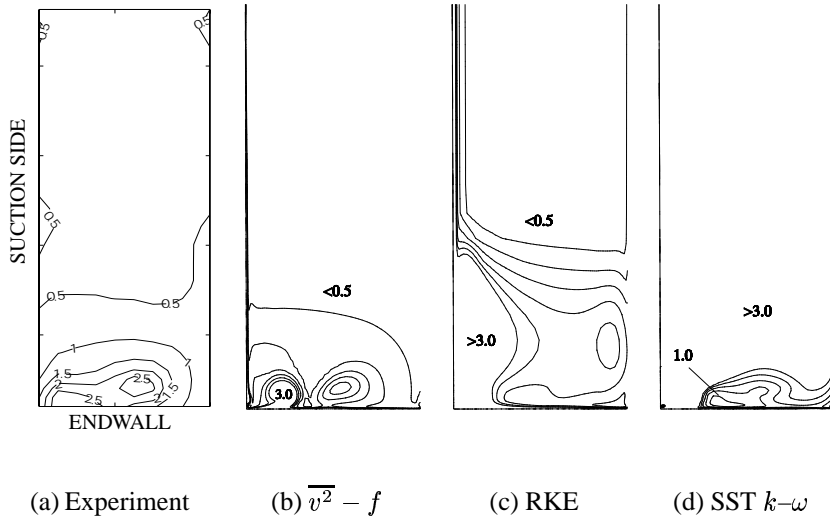
60

(a) Experiment       (b) $\overline{v^2} - f$       (c) RKE       (d) SST $k$–$\omega$

Figure 4.11: Predicted levels of turbulent kinetic energy in plane SS (cf. Figure 4.9) using three FLUENT turbulence models. Contour intervals of 0.5.

amount entering at the inlet of the computational flow domain. As already mentioned several times eddy-viscosity based turbulence models often give too high levels of eddy viscosity in stagnation regions as the production of $k$ is overpredicted. If this is the case the high levels of $k$ will be convected downstream the passage and should be clearly visible in plane SS. Therefore the contours of $k$ in this plane are compared with experimental data in Figure 4.11.

Indeed, the distribution of $k$ for the different models do differ a lot. The most outstanding result is seen in Figure 4.11(d), obtained with the SST $k - \omega$ model. In almost the entire plane the level of turbulent kinetic energy exceeds $3.0 \, m^2/s^2$, which is to be compared with experimental freestream value that is below $0.5 \, m^2/s^2$. This is unquestionably the effect of a huge overprediction of the stagnation region production of $k$. In the $\overline{v^2} - f$ model and the Realizable $k - \varepsilon$ model it seems that this problem partly has been solved. In the Realizable $k - \varepsilon$ model there is still a region in the upper left corner where one can suspect that the levels are too high due to the stagnation point anomaly. Of greater importance is the region closer to the endwall where the two models give very different predictions. By comparison with the experiment it is obvious that the RKE model give too high levels of $k$, especially in the lower left corner, whereas the $\overline{v^2} - f$

61

model prediction agree reasonably well throughout the whole plane. The largest mismatch of the $\overline{v^2} - f$ computation compared to experiment is the center of the suction side horseshoe vortex. The levels in the passage vortex on the other hand are close to the measurements. All in all, the by far best prediction of the turbulent kinetic energy in plane SS was obtained with the $\overline{v^2} - f$ model.

## 4.2.2 The Influence of Realizability on the Secondary Flow Field

In Section 4.1.2 it was shown that the realizability constraint had strong influence on the level of all turbulent quantities that where investigated. With the findings of the previous section in mind we will now consider how the secondary flow is affected by the model constant $C_{lim}$, which determines the strength of the bound on the turbulent time scale. The turbulence model used in this numerical "experiment" is Model 1.

The secondary velocities of these computations are shown in Figure 4.12 along with the result of the $\overline{v^2} - f$ model used in FLUENT, which can be considered as a benchmark as it gave the best results of the FLUENT models. Three different levels of $C_{lim}$ where tried; $\infty$, i.e. no constraint at all, 1.0 and 0.6.

The results indicate that the secondary velocities is not that sensitive to the realizability constraint. However, as one might expect, the secondary motion is somewhat weakened due to the extra viscosity produced when the constraint is turned off. The differences when using $C_{lim} = 1.0$ and $\infty$ are hardly distinguishable and FLUENT and the $C_{lim} = 0.6$ case give almost identical results. Note that for the CALC-BFC computations Model 1 was used. This model uses the non-zero $f$ wall boundary condition, whereas the $\overline{v^2} - f$ model implemented in FLUENT uses a $f = 0$ wall boundary condition. Hence, the latter is likely Model 2 or 3 (which essentially are the same model). This indicates that the only effect the reformulation by Lien & Kalitzin (2001) has on the original $\overline{v^2} - f$ model is the desired effect of making the $f$ wall boundary condition more stable.

The effect of the realizability constraint on the turbulent kinetic energy in plane SS is shown in Figure 4.13, where the $k$ distribution is given for same computations as in Figure 4.12. Here it is more obvious that the choice of $C_{lim}$ is important also in $\overline{v^2} - f$ models and that the model's improved physical foundation compared to two-equation models does not solve the problem of the stagnation point anomaly. Note that the high levels of $k$ (and $\nu_t$) in plane SS2 only seems to have little effect on the secondary structures. Later it will be shown that the
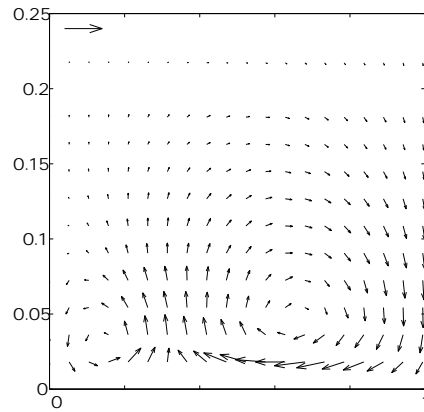
62
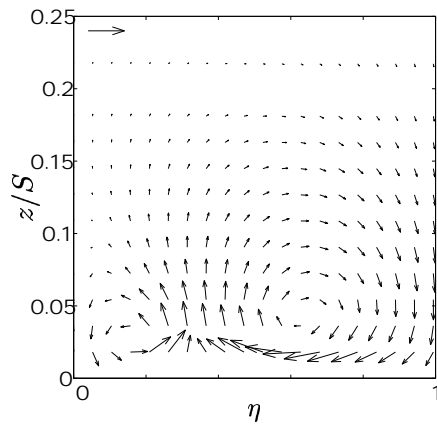
(a) FLUENT $\overline{v^2} - f$
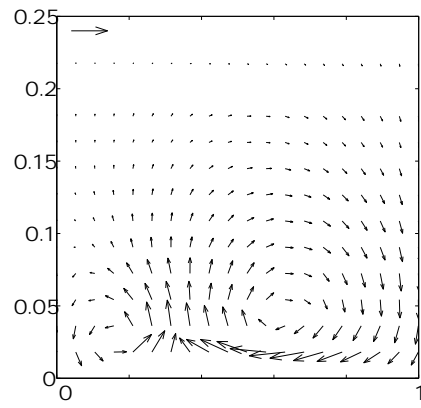
(b) Model 1 $C_{lim} = 0.6$
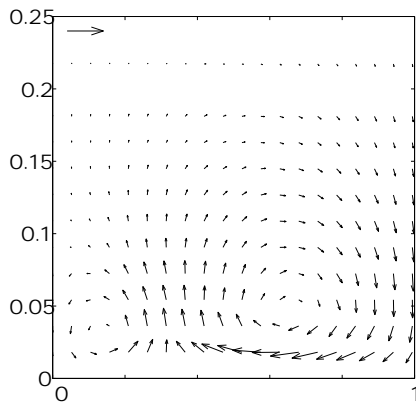
(c) Model 1 $C_{lim} = \infty$

(d) Model 1 $C_{lim} = 1.0$

Figure 4.12: Calculated secondary velocities in the lower half of plane SS (cf. Figure 4.9). Endwall located at $z = 0$. Suction and pressure surfaces located at $\eta = 0$ and $\eta = 1$, respectively. The arrow in the upper left corner corresponds to $\frac{5}{35}U_\infty$.

63

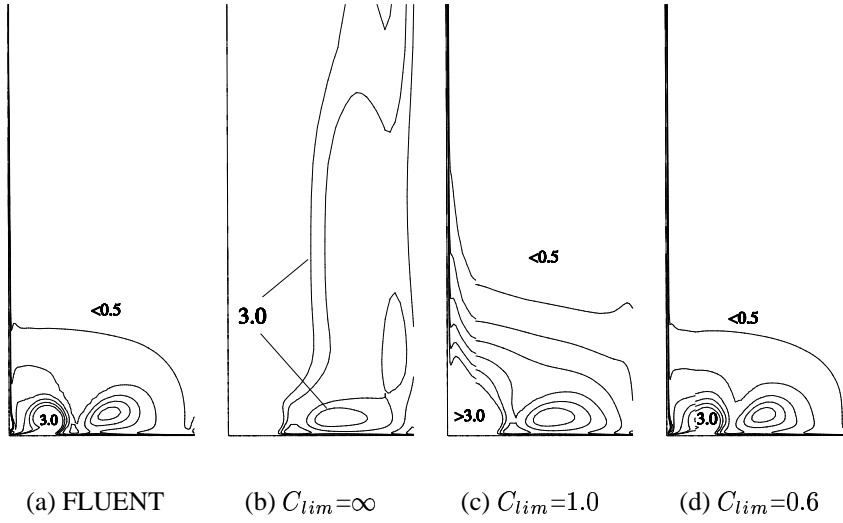(a) FLUENT      (b) $C_{lim}=\infty$      (c) $C_{lim}=1.0$      (d) $C_{lim}=0.6$

Figure 4.13: Measured and predicted levels of turbulent kinetic energy in plane SS. Comparison of FLUENT and three CALC-BFC computations with different $C_{lim}$. Contour intervals of 0.5.

intensity of the secondary motion in the vane passage is largely determined by how well the flow in the stagnation region is predicted.

In Figure 4.13(b), where the constraint is not used, the levels of $k$ are greater than 3.0 $m^2/s^2$ in almost the entire plane with the exception of a region to the right where $k$ is slightly lower ($\approx 2.5\ m^2/s^2$). Setting the value of $C_{lim}$ to 1.0, i.e. using the time scale bound that can be algebraically derived, improves the prediction a great deal. Further reducing the value of $C_{lim}$ to 0.6 gives levels of $k$ that are very close to experiments as well as the predictions of the FLUENT $\overline{v^2} - f$ model.

It is interesting that even if $k$ is very sensitive to the choice of the model constant $C_{lim}$ the value of 0.6 does give fairly accurate predictions of $k$ in the stator vane test case of this study. This value has not been tuned to fit this particular set of experimental data but can be found in several investigations by other researches, e.g. Lien & Kalitzin (2001), Kalitzin (1999), which suggests that this value has a potential of being applicable to a wider range of flows.

### 4.2.3   Comparison of the $\overline{v^2} - f$ Model Versions

One of the objectives of this work was to compare the three $\overline{v^2} - f$ turbulence models given in Section 2.3.3. Due to severe convergence problems when using the standard realizability constraint ($C_{lim}$=0.6) in Model 2 it became rather difficult to make a valuable model comparison. For the coarse mesh (about 500,000 cells) computations with Model 2 and 3 diverged as soon as the time scale bound was used in the $f$ equation. Therefore the comparison was carried out without using this bound in the $f$ equation and one may ask whether the comparison then is of any use.

In order to show that it really is, two additional computations were performed with Model 1, one including the time scale bound in the $f$ equation, labelled C in Figure 4.14, and one without this bound, labelled B. The flow field variable chosen for comparison is the spanwise mean velocity component, $W$, and the turbulent kinetic energy, $k$. They are plotted along a line 2 cm above the vane endwall in plane SS, a location approximately at the center of the secondary flow structures. As can be seen from this figure the results of these two computations give almost identical results. The conclusions of this result is that it is of minor importance whether the realizability constraint is used in the $f$ equation or not and that the different models can be compared without the use of this bound.

Even with this modification a fully converged solution was never achieved with Model 2. The Model 3 computation, labelled C, on the other hand did converge and is included in Figure 4.14. The match between cases A, B and C are as good as perfect and it can be concluded that Model 1 and 3 give very similar results, particularly in terms of the secondary flow field. For reference the corresponding spanwise velocity profile from the FLUENT Realizable $k - \varepsilon$ computation is included. As already mentioned this model gives a much weaker secondary motion.

Worth mentioning is that Model 2 did converge on a finer mesh, which was used when investigating grid independence, with the slight modification that $\varepsilon/k$ in the $\overline{v^2}$ equation was replaced with $1/\mathcal{T}$. Of course the same change was tried on the coarse mesh but without success. This suggests that $\overline{v^2} - f$ models in general and Model 2 in particular are sensitive to the quality of the mesh, especially in the near-wall region. Another observation is that the increased levels of $\overline{v^2}$ in regions very close to walls, where $k/\varepsilon$ in the $\overline{v^2}$ equation is replaced with $6\sqrt{\nu/\varepsilon}$, in the present simulations stabilizes the solution.
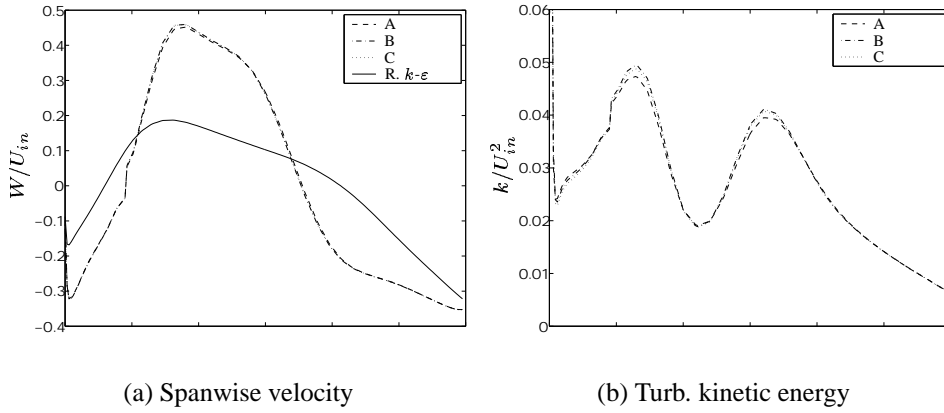
(a) Spanwise velocity       (b) Turb. kinetic energy

Figure 4.14: Spanwise velocity for different $\overline{v^2} - f$ model versions at a line 2 cm above the endwall in plane SS. A) Model 3 without realizability constraint in the $f$ equation. B) Same as A but Model 1. C) Same as B but with realizability constraint in the $f$ equation.

## 4.2.4 The Stagnation Region Flow Field

As mentioned above the prediction of the secondary flow field in the stagnation region, which indeed is the area from where the horseshoe vortex system originates, is important for this type of flow. And, as illustrated in Section 4.1.2, the realizability constraint has a strong impact on the stagnation region distribution of turbulent quantities. In this section the performance of different FLUENT turbulence models and the role of the realizability constraint in the stagnation region is examined.

**FLUENT**

In Figure 4.15 contours of the turbulent kinetic energy are shown for four FLUENT computations using different turbulence models. Just as for the SS plane the results among the models differ substantially, again the SST $k - \omega$ model standing out the most. From Figure 4.15(d) it is obvious that the strong retardation (large $S_{11}$ and, from continuity, $S_{22}$) of the flow as it approaches the stagnation point has caused the production of turbulent kinetic energy to be very high. The other three models give more similar results but are still quite different from each other. Unfortunately experimental data needed to determine which of these models
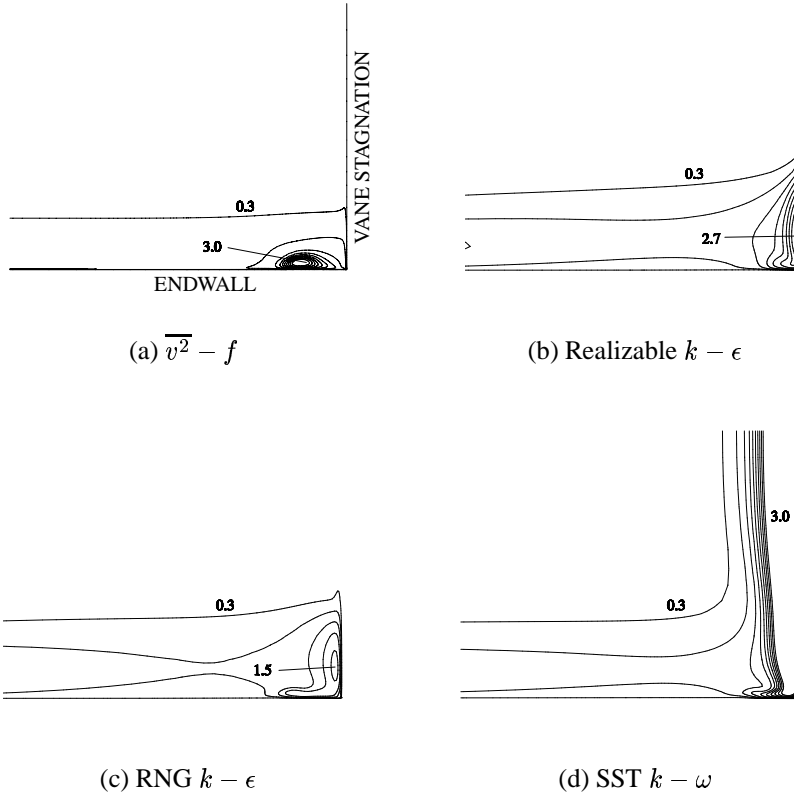
66

PSfrag replacements

ENDWALL    VANE STAGNATION

PSfrag replacements

VANE STAGNATION

ENDWALL

0.3

3.0

0.3

2.7

(a) $\overline{v^2} - f$

(b) Realizable $k - \epsilon$

PSfrag replacements

ENDWALL

VANE STAGNATION

PSfrag replacements

ENDWALL

VANE STAGNATION

0.3

1.5

0.3

3.0

(c) RNG $k - \epsilon$

(d) SST $k - \omega$

Figure 4.15: Contours of turbulent kinetic energy in the stagnation plane STAG1 (cf. Figure 4.9) for some FLUENT computations. Contour intervals of $0.3 m^2/s^2$

that perform the best in terms of stagnation region $k$ are not available. However, in Figure 4.16 the result of a computation and corresponding measurements of a similar flow, the flow around a wall mounted appendage (a symmetrical wing profile mounted on a flat surface), is included. It can be seen that the $\overline{v^2} - f$ model implemented in FLUENT give very good agreement with experiment and that the stagnation $k$ distribution of this flow is very similar to the result in Figure 4.15(a). The $k$ contours of the Realizable $k - \varepsilon$ and the RNG $k - \varepsilon$ (Figures 4.15(b) and 4.15(c)) models do have about the same shape but differ in magnitude, the former having a maximum almost twice as high as the latter. The main difference from the $\overline{v^2} - f$ model prediction is that the location of the maximum is just above the *vane* wall instead of lying slightly above the *endwall*.
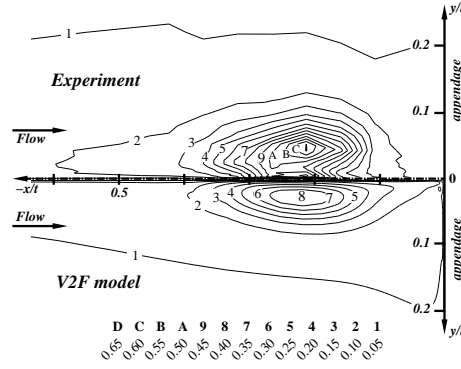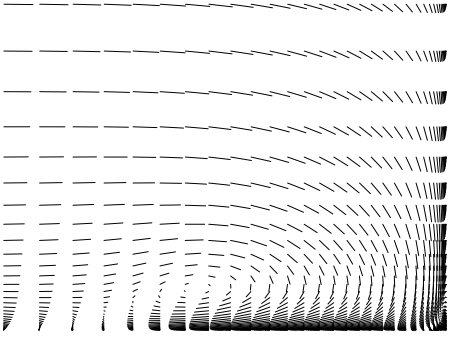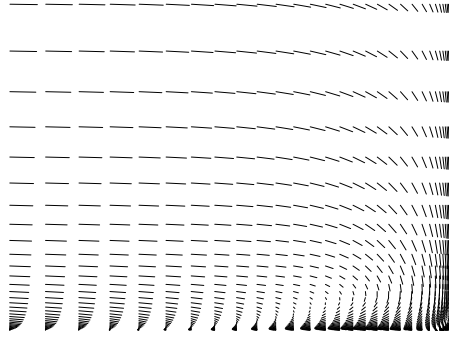
Figure 4.16: Comparison of measured and predicted (using the $\overline{v^2} - f$ model) stagnation region turbulent kinetic energy for the flow around a wall-mounted appendage (Parneix & Durbin (1997)).

The effect this has on the mean flow can be seen in Figure 4.17, where the mean velocity vectors are plotted in the stagnation plane. Note that the plots in this figure do not show the complete stagnation plane but only a limited region close to the vane/endwall junction. For comparison, the position of the center of the $\overline{v^2} - f$ stagnation vortex (Figure 4.17(a)) corresponds very well to the location of its maximum level of kinetic energy (Figure 4.15(a)). The high $k$ (and $\nu_t$) predicted by the two $k - \varepsilon$ models above the vane wall has the effect that the recirculating motion in this region is restrained by the diffusive eddy-viscosity momentum transport. As this motion is part of the stagnation vortex roll-up the extra viscosity also decreases the intensity of the horseshoe vortex. This explains why the RNG $k - \varepsilon$ model, which has somewhat lower levels of $k$, predicts a stronger secondary motion than the Realizable $k - \varepsilon$ model. Not very surprisingly the $\overline{v^2} - f$ model, which gave the strongest vortices in plane SS, also predicts a more intense horseshoe vortex roll-up in the stagnation region than the other models do.

Another important issue is how the heat transfer to the endwall is affected by the horseshoe vortex. If this vortex is of high intensity it will tear up the incoming, insulating boundary layer and replace the relatively cold fluid close to the endwall with hot gas from the freestream region. An example of this phenomenon is seen in Figure 4.17(a) where the flow is directed downwards in between the horseshoe vortex and the stator vane (see also the streamlines in Figure 3.4). In order to see the influence this has on the heat transfer the predicted Stanton number distribu-
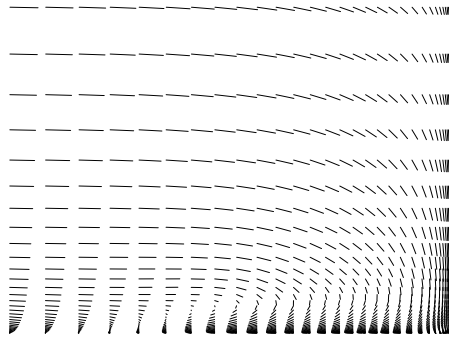
68

(a) $\overline{v^2} - f$

(b) Realizable $k - \epsilon$
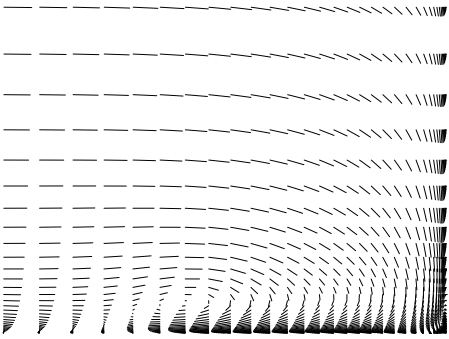
(c) RNG $k - \epsilon$

(d) SST $k - \omega$

Figure 4.17: Velocity vectors in the stagnation plane STAG2 (cf. Figure 4.9) for some FLUENT computations showing the horse-shoe vorte roll-up.
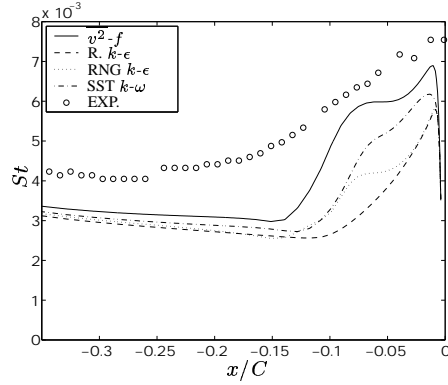
Figure 4.18: Comparison of measured and predicted (using FLUENT) Stanton number along the endwall stagnation line.

tion along the endwall stagnation line is plotted in Figure 4.18 for the FLUENT computations.

From Figure 4.18 two important conclusions can be drawn. In all cases the heat transfer in the region well upstream the stator vane is underestimated by some 30%. This is probably due to the inlet boundary layer profiles of the turbulent quantities not being fully consistent with the experimental setup. Unfortunately, the inlet profiles of $k$ and $\overline{v^2}$ needed to verify this are not available. Secondly, the heat transfer in the region of the horseshoe vortex roll-up seems to be independent of the inlet conditions. Instead it is determined by the intensity of the vortex itself, which is in line with the above discussion on hot/cold gas exchange. Therefore, the $\overline{v^2} - f$ prediction of the heat transfer lies much closer to the level found in measurements all along the stagnation line. When the initial mismatch between the experiments and the $\overline{v^2} - f$ model is outweighed by the presence of the vortex the agreement is very good, the $\overline{v^2} - f$ model giving about 10% too low values. Due to the other models' inability to reproduce the strength of the vortex they also fail to predict the correct level of heat transfer giving values some 30–50% too low. In all computations the $y^+$ values along the stagnation line is about 0.2.

**Effects of Realizability**

As already mentioned the realizability constraint did not have as strong influence on the secondary motion as one might expect. The kinetic energy predictions on the other hand were improved be using the constraint. In Figure 4.19 contours of $k$ are plotted in the stagnation plane for different values of $C_{lim}$. The results are in

70

line with the conclusions drawn earlier. $C_{lim} = \infty$ gives too high production of $k$ and when $C_{lim}$ is set to 0.6 the agreement with the FLUENT $\overline{v^2} - f$ model is almost perfect. However, as all the $\overline{v^2} - f$ model versions give rather good predictions of the secondary motion even when the levels of $k$ are very high, this suggests that it is not only the level of $k$ that is important but also that the formulation of the $\overline{v^2} - f$ model has some other feature that makes it more suitable for stagnation point flows than other two-equation turbulence models. For example, by comparing Figures 4.19(b) and 4.15(b) one would expect a weaker secondary motion in the former case as $k$ here is higher in most of the region, but by inspection of Figures 4.12(c) and 4.10(c) we see that this is not the case.

Finally, contours of the computed eddy viscosity in the stagnation plane are shown in Figure 4.20 for values of $C_{lim}$ of $\infty$ and 0.6. As was the case in the two-dimensional computations the location where the constraint is activated is immediately identified and as the flow reaches the vane stagnation the level of the eddy viscosity has been reduced by more than 90%! As the turbulent heat transport is modelled using a diffusive eddy-viscosity hypothesis the effect of the realizability of vane heat transfer is likely to be profound.

## 4.3 Endwall Effects at Midspan

Due to the great reduction of computational requirements when going from a full three-dimensional computation to two dimensions this is a commonly used assumption when analyzing turbomachinery flows. When making this assumption, i.e. that the vane profile is infinitely long, any influence of the endwalls on the flow at midspan of the vane is neglected. Whether this approximation is appropriate or not should be confirmed by running a three-dimensional computation of the "real", finite, geometry. This is especially important in this case as the experiment was designed to produce a thick incoming boundary layer in order to have rather large, measurable, secondary flow structures at the vane endwall. The issue is that the larger the structures, the further away from the endwall the effect of the secondary flow will be visible. Whether or not this is a problem in this case will be illustrated below.

Figure 4.21(a) shows contours of the velocity magnitude, $|\underline{V}| = (U^2 + V^2 + W^2)^{1/2}$, downstream a stator row in a plane, P2, normal to the mean flow direction (the location of the plane is given in Figure 4.21(b)). The flow at the top of the domain, i.e. around midspan, seems to be very close to two-dimensional. Now the velocity $|\underline{V}|$ along the midspan line of this plane (the values at the very top
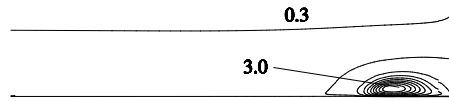
71
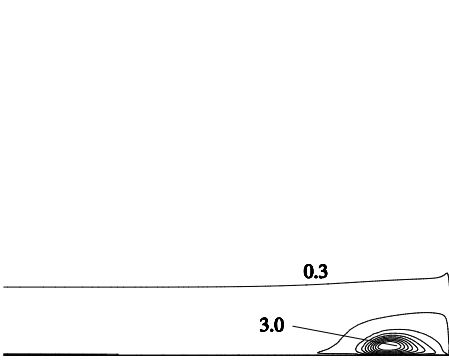
(a) FLUENT
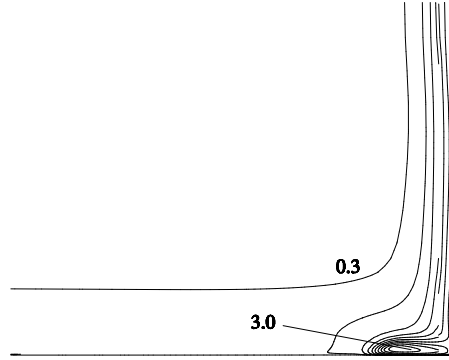
(b) Model 1, $C_{lim} = \infty$
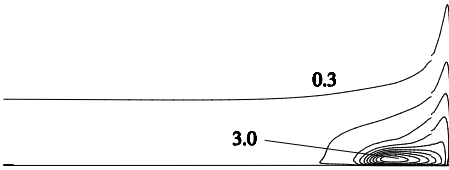
(c) Model 1, $C_{lim} = 1.0$

(d) Model 1, $C_{lim} = 0.6$

Figure 4.19: Contours of turbulent kinetic energy in the stagnation plane STAG1 (cf. Figure 4.9 and 4.15) for different $\overline{v^2} - f$ computations. Contour intervals of $0.3\ m^2/s^2$

MIDSPAN

PSfrag replacements

175

INLET

MIDSPAN

ENDWALL

VANE STAG.

250

250

ENDWALL

VANE STAG.

INLET

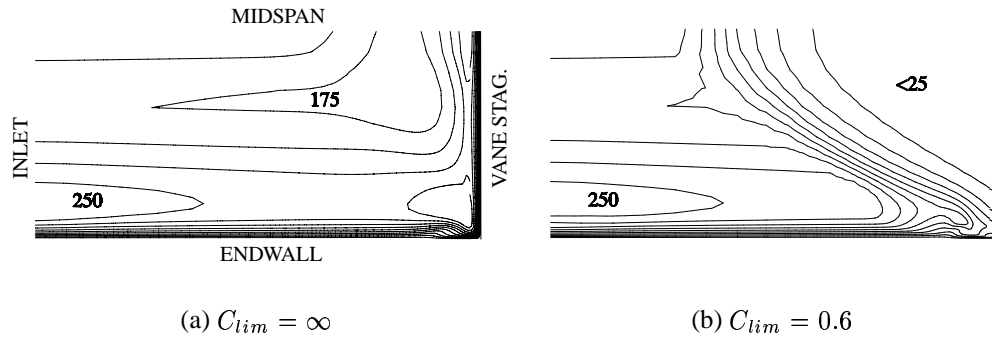<25

(a) $C_{lim} = \infty$

(b) $C_{lim} = 0.6$

Figure 4.20: The effect of realizability on the turbulent viscosity in the stagnation plane

of the plane) is compared to the corresponding velocity profile taken from a two-dimensional computation (using the same mesh and the same turbulence model). The results are shown in Figure 4.22(a), which illustrates a difference between the two- and three-dimensional simulations. If there is a difference at midspan caused by the presence of the endwall the endwall must have affected the flow in the entire vane passage. We see that in the three-dimensional computation the midspan velocity has decreased. This is because the secondary flow has flattened out the initially thick boundary layer, allowing for a net spanwise fluid transport. This effect is important as most turbulence models are tuned using experiments that are supposed to accurately represent the assumption of two-dimensionality. In Figure 4.22(b) the net fluid transport in the spanwise direction is illustrated by contours of the $z$-component of the mean velocity in plane P1 defined in Figure 4.21(a). To the right of the contour line "0.0", which is the larger part of the plane, we find the downward motion explaining why the midspan total velocities of the three-dimensional computation are lower than in the two-dimensional analysis. The arrows indicate the direction of the net fluid motion caused by the secondary flow structures at the vane endwall.

## 4.4 Grid Independence

In order to investigate, for example, the performance of a turbulence model in a certain fluid flow one must somehow reassure that the obtained results will not

73
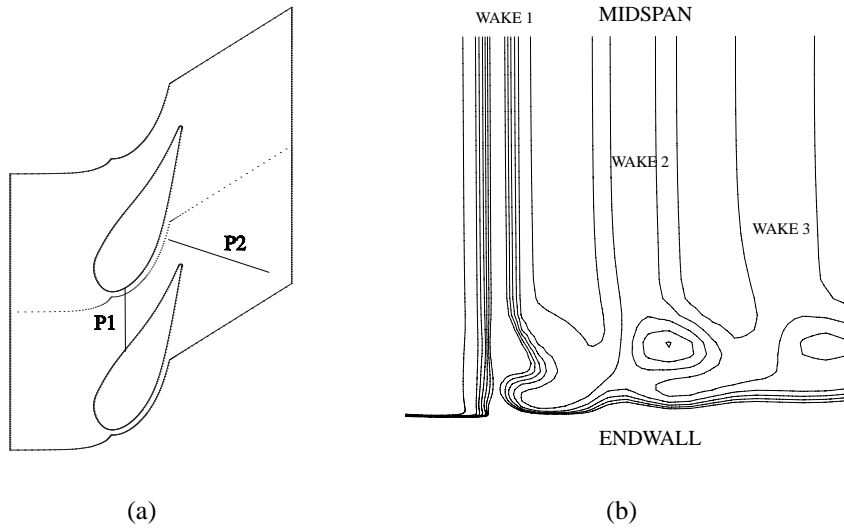
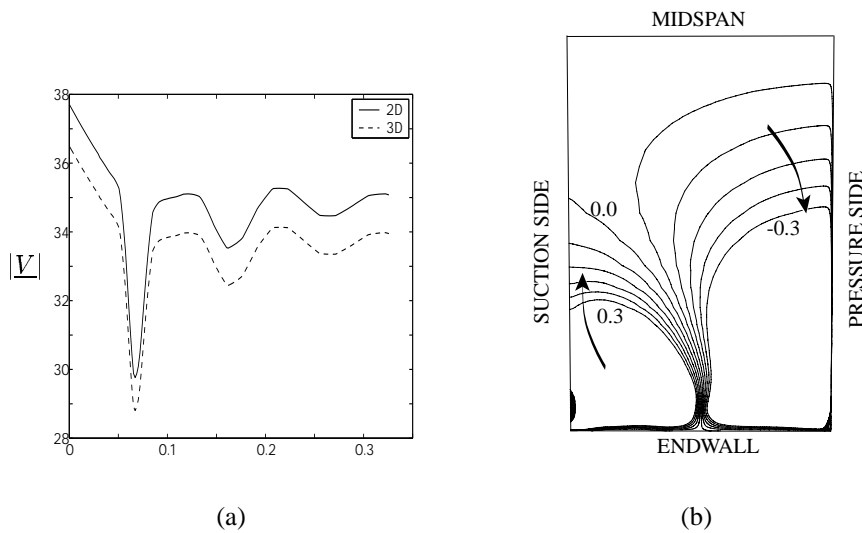Figure 4.21: a) Location of planes P1 and P2. b) Contours of velocity magnitude in plane P2.



Figure 4.22: a) Comparison of predicted velocity magnitude at the midspan line of plane P2 for two- and tree-dimensional computations. b) Contours of the spanwise velocity component (from 3D computation) in plane P1 (cf. Figure 4.21(a)). The arrows indicate the net transport i the $z$ direction.
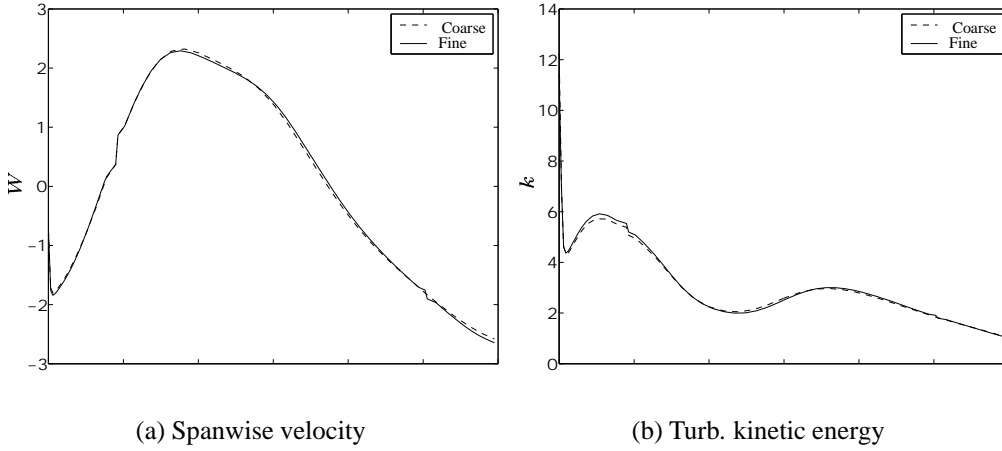
74

(a) Spanwise velocity           (b) Turb. kinetic energy

Figure 4.23: Profiles of the spanwise mean velocity, $W$, and the turbulent kinetic energy, $k$, along a line 2 cm above the endwall in plane SS for two different meshes.

alter if the resolution of the computational grid is increased. For instance, if the computed results differ from experiments one cannot be sure if the scatter is due to an inaccurate physical model or due to insufficient grid resolution unless the numerical results is reproduced on a refined grid.

In Figure 4.23 the results of a grid independence study are shown. As a main focus of this work is on the secondary flow structures in the vicinity of the stator endwall, the profile of the spanwize velocity component, $W$, 2 cm above the endwall in plane SS is given in Figure 4.23(a). This line goes straight across the vortices shown in for example Figure 4.12(a). The reason why $W$ was chosen is that this component is a result of the secondary flow and would have been zero if the vane/endwall flow interaction was not resolved. The coarse and fine grid consist of about 500,000 and 1,700,000 computational cells, respectively. It can be seen that the coarse mesh is fine enough to resolve the secondary flow. To make sure that the turbulent quantities too are grid independent $k$ is plotted along the same line in Figure 4.23(b). The result is satisfactory and the conclusion is that the coarse grid is fine enough for this type of computation.

# Chapter 5

# Summary of Results

In this study the performance of three different versions of the $\overline{v^2} - f$ model in a stator vane passage flow was investigated. It was found that all three models gave very similar results, particularly in terms of predicting the secondary flow originating from the vane/endwall junction, known as the horseshoe vortex system. The $\overline{v^2} - f$ model was found to be able to predict the presence of some of the vane passage vortices, but in general gave somewhat too low intensities of the swirling motion compared to experimental data.

Also the capability of the eddy-viscosity based turbulence models in the commercial software FLUENT to predict the vane passage flow was examined. Of the available models the $\overline{v^2} - f$ model, followed by the RNG $k - \varepsilon$ model, was found to give the best agreement with measurements. The worst results, in terms of predicting the secondary flow, was obtained with the Realizable $k - \varepsilon$ model. It was also found that the FLUENT $\overline{v^2} - f$ version and the three models implemented in CALC-BFC gave almost identical results.

The influence of the realizability constraint, originally suggested by Durbin (1995*b*), on the development of the secondary motion in a stator vane passage has also been investigated. The results of all computations involving stagnation regions show that the predictions of all flow properties, in particular the turbulent kinetic energy, is significantly improved by the use of the realizability constraint. One consequence of not using the constraint was that the intensity of the secondary motion, which has a strong impact on endwall heat transfer in a vane passage, was weakened.

In Section 2.4 the mechanisms of the realizability constraint when used in conjunction with the $\overline{v^2} - f$ turbulence model were analyzed and it was shown that the standard formulation of the $\overline{v^2} - f$ model is inconsistent in farfield regions

77

when the constraint is active. In some cases this inconsistency caused numerical difficulties. It was also shown that this problem could be solved by slightly modifying the original $\overline{v^2} - f$ model formulation. Three different modifications to the $\overline{v^2}$ and $f$ equations were suggested, which all improved the numerical stability seemingly without affecting the mean flow results. This indicate the use of realizability constraint in the $\overline{v^2}$ and $f$ equations is of minor importance.

Finally, the FLUENT predictions of the endwall stagnation region heat transfer were compared with experiments. All models gave similar but too low estimates of the heat transfer in the region upstream the vane. This discrepancy is likely due to inconsistencies between experiments and the prescribed inlet boundary conditions in the computations. However, as the vane is approached the influence of the inlet conditions is outweighed by the presence of the horseshoe vortex, which significantly increases the heat transfer to the endwall. In this region the $\overline{v^2} - f$ model, which rather accurately predicted the secondary motion, gave results that agreed well with experiments.

## 5.1   Future Work

The influence of the prescribed turbulent quantities at the inlet of the computations needs to be investigated as the profiles specified were not available from experiments. Another uncertainty is the location of the inlet. A rule of thumb should be established for the distance needed between the leading edge and the inlet of the computational domain in order for the flow to be unaffected by the inlet location.

The ability of the $\overline{v^2} - f$ model in predicting complex flow in general and heat transfer in particular needs further validation. This can to some extent be done by simulating the additional cases offered by the data set already used in this work, which would allow for studying the influence of freestream turbulence and Reynolds number. Preferably, additional validation against less complex, reliable test cases relevant for turbomachinery applications, like vane heat transfer in transonic flows, should be carried out. This type of well documented studies are needed in order to determine the applicability of the so far promising $\overline{v^2} - f$ model to a wider range of flows.

Recently, a non-linear $\overline{v^2} - f$ model taking into account the anisotropy when calculating heat transfer has been proposed. The prospect of improving heat transfer predictions based on this approach can easily be investigated by solving the temperature equation based on the flow field given by a linear $\overline{v^2} - f$ computation.

Finally, it is believed that the complex flow existing in stator vane passages have important unsteady features that cannot be resolved using steady RANS simulations. This is supported by experiments, which, for example, indicate that the leading edge horseshoe vortex is oscillating at a certain frequency. If this is the case the heat transfer to the endwall in this region can in general not be predicted by a steady state solution approach. Therefore, it is suggested that the next step in trying to improve flow and heat transfer predictions is to account for instationary effects using unsteady RANS (URANS).

# Bibliography

AMES, F. 1997 The influence of large-scale high-intensity turbulence on vane heat transfer. *Journal of Turbomachinery* **119**, 23–30.

AMES, F. & PLESNIAK, M. 1997 The influence of large-scale high-intensity turbulence on vane aerodynamic losses, wake growth and exit turbulence parameters. *Journal of Turbomachinery* **119**, 182–192.

ARTS, T., DE ROUVRIOT, M. L. & RUTHERFORD, A. 1990 Aero-thermal investigation of a highly loaded transonic linear turbine guide vane cascade. *Technical Report 174* .

BOYLE, R. & RUSSELL, L. 1990 Experimental determination of stator endwall heat transfer. *Journal of Turbomachinery* **112**, 547–558.

BRADSHAW, P. 1996 Turbulence modelling with application to turbomachinery. *Proc. Aerospace Science* **32**, 575–624.

DAVIDSON, L. & FARHANIEH, B. 1995 CALC-BFC: A finite-volume code employing collocated variable arrangement and cartesian velocity components for computation of fluid flow and heat transfer in complex three-dimensional geometries. Rept. 95/11. Dept. of Thermo and Fluid Dynamics, Chalmers University of Technology, Gothenburg.

DAVIDSON, L., NIELSEN, P. V. & SVENINGSSON, A. 2003 Modifications of the $v^2 - f$ model for computing the flow in a 3d wall jet (to be presented). In *4th Int. Symp. on Turbulence Heat and Mass Transfer*. Antalya, TURKEY.

DUNN, M. 1990 Phase and time-resolved measurements of unsteady heat transfer and pressure in a full-stage rotating turbine. *Journal of Turbomachinery* **112**, 531–538.

DUNN, M., RAE, W. & HOLT, J. 1984 Measurement and analyses of heat flux data in a turbine stage: Part ii—discussion of results and comparison with predictions. *Journal of Engineering for Gas Turbines and Power* pp. 234–240.

DURBIN, P. 1991 Near-wall turbulence closure modeling without 'damping functions'. *Theoretical and Computational Fluid Dynamics* **3**, 1–13.

DURBIN, P. 1993 Application of a near-wall turbulence model to boundary layers and heat transfer. *International Journal of Heat and Fluid Flow* **14**, 316–323.

DURBIN, P. 1995*a* On the $k$-3 stagnation point anomaly. *International Journal of Heat and Fluid Flow* **17**, 89–90.

DURBIN, P. 1995*b* Separated flow computations with the $k - \epsilon - v^2$ model. *AIAA Jounal* **33**, 659–664.

ERIKSSON, L. 2002 private communication. Dept. of Thermo and Fluid Dynamics, Chalmers University of Technology, Göteborg, Sweden.

GEORGE, W. 2000 private communication. Dept. of Thermo and Fluid Dynamics, Chalmers University of Technology, Göteborg, Sweden.

GIEL, P., FOSSEN, R. V., BOYLE, R., THURMAN, D. & CIVINSKAS, K. 1999 Blade heat transfer measurements ans predictions in a transonic turbine cascade. NASA/TM—1999-209296.

GIEL, P., THURMAN, D., FOSSEN, R. V., HIPPENSTEELE, S. & BOYLE, R. 1998 Endwall heat transfer measurements in a transonic turbine cascade. *Jounal of Turbomachinery* **120**, 305–313.

GIEL, P., THURMAN, D., LOPEZ, I., BOYLE, R., FOSSEN, R. V., JETT, G., CAMPERCHIOLI, T. & LA, H. 1996 Three-dimensional flow field measurements in a transonic turbine cascade. *ASME paper No. 96-GT-113* .

GRAZIANI, R., BLAIR, M., TAYLOR, J. & MAYLE, R. 1980 An experimental study of endwall and airfoil surface heat transfer in a large scale turbine blade cascade. *Journal of Engineering for Power* **102**, 257–267.

HARVEY, N., ROSE, M., COUPLAND, J. & JONES, T. 1999 Measuremement and calculation of nozzle guide vane end wall heat transfer. *Journal of Turbomachinery* **121**, 184–190.

HERMANSON, K. & THOLE, K. 2000*a* Effect of inlet conditions on endwall secondary flows. *Journal of Propulsion and Power* **16**, 286–296.

HERMANSON, K. & THOLE, K. 2000*b* Effect of mach number on secondary flow characteristics. *International Journal of Turbo and Jet Engines* **17**, 179–196.

HUNT, J., WRAY, A. & MOIN, P. 1988 Eddies, stream, and convergence zones in turbulent flows. *Center for Turbulence Research Report CTR-S88* p. 193.

IACCARINO, G. 2001 Predictions of a turbulent separated flow using commercial cfd codes. *Journal of Fluids Engieering* **123**, 819–828.

JEONG, J. & HUSSAIN, F. 1995 On the identification of a vortex. *Journal of Fluid Mechanics* **285**, 69–94.

JOHANSSON, T. 2002 private communication. Dept. of Thermo and Fluid Dynamics, Chalmers University of Technology, Göteborg, Sweden.

JONES, W. & LAUNDER, B. 1972 The prediction of laminarization with a two-equation model of turbulence. *Int. J. of Heat and Mass Transfer* **15**, 301–314.

KALITZIN, G. 1999 Application of the $\overline{v^2} - f$ model to aerospace configurations. Center for Turbulence Research Annual Research Breifs.

KANG, M., KOHLI, A. & THOLE, K. 1999 Heat transfer and flowfield measurements in the leading edge region of a stator vane endwall. *Journal of Turbomachinery* **121**, 558–568.

KANG, M. & THOLE, K. 2000 Flowfield measurements in the endwall region of a stator vane. *Journal of Turbomachinery* **122**, 458–466.

KATO, M. & LAUNDER, B. 1993 The modelling of turbulent flow around stationary and vibrating square cylinders. In *Ninth Symposium on Turbulent Shear Flows*, pp. 10–4–1–10–4–6.

LANGSTON, L., NICE, M. & HOOPER, R. 1977 Three-dimensional flow within a turbine cascade passage. *Journal of Engineering for Power* **99**, 21–28.

LAUNDER, B., REECE, J. & RODI, W. 1975 Progress in development of a reynolds-stress turbulence closure. *Journal of Fluid Mechanics* **68**, 537–566.

83

LIEN, F. & KALITZIN, G. 2001 Computations of transonic flow with the $\overline{v^2}$-$f$ turbulence model. *International Journal of Heat and Fluid Flow* **22**, 53–61.

MANCEAU, R., WANG, M. & LAURENCE, D. 2001 Inhomogeneity and isotropy effects on the redistribution term in reynolds-averaged navier-stokes modelling. *Journal of Fluid Mechanics* **438**, 307–338.

MANSOUR, N., KIM, J. & MOIN, P. 1988 Reynolde-stress and dissipation-rate budgets in a turbulent channel flow. *Journal of Fluid Mechanics* **194**, 15–44.

MAYLE, R., DULLENKOPF, K. & SCHULTZ, A. 1998 The turbulence that matters. *Journal of Turbomachinery* **120**, 402–409.

MOSER, R., KIM, J. & MANSOUR, N. 1999 Dns of turbulent channel flow up to re$_\tau = 590$. *Physics of Fluids* **11**, 943–945.

NILSSON, H. 2002 Numerical investigations of turbulent flow in water turbines. PhD thesis, Dept. of Thermo and Fluid Dynamics, Chalmers University of Technology, Göteborg, Sweden.

PARNEIX, S. & DURBIN, P. 1997 Numerical simulation of 3d turbulent boundary layers using the $\overline{v^2} - f$ model. Center for Turbulence Research Annual Research Breifs.

PARNEIX, S., DURBIN, P. & BEHNIA, M. 1998 Computation of 3-d turbulent boundary layers using the v2f model. *Flow, Turbulence and Combustion* **60**, 19–46.

PATEL, C., RODI, W. & SCHEUERER, G. 1985 Turbulence models for near-wall and low reynolds number flows: A review. *AIAA Jounal* **23**, 1308–1319.

RADOMSKY, R. 2000 High freestream turbulence studies on a scaled-up stator vane. PhD thesis, University of Wisconsin-Madison.

RADOMSKY, R. & THOLE, K. 2000*a* Flowfield measurements for a highly turbulent flow in a stator vane passage. *Journal of Turbomachinery* **122**, 255–262.

RADOMSKY, R. & THOLE, K. 2000*b* Measurements and predictions of a highly turbulent flowfield in a turbine vane passage. *Journal of Fluids Engineering* **122**, 666–676.

RUBENSDÖRFFER, F. 2002 Literature survey: Vane and blade secondary flow and endwall heat transfer. Rept. kth-hpt-37/02. Dept. of Energy Technology, Royal Insitue of Technology, Stockholm.

SAVILL, A. 2001 private communication. von Karman Institue for Fluid Dynamics.

SAVILL, A. 2002*a* By-pass transition using conventional closures. In *Recent Development in Numerical methods for Turbomachinery Flows*. von Karman Institue for Fluid Dynamics, lecture Notes 2002-01.

SAVILL, A. 2002*b* New strategies in modelling by-pass transition. In *Recent Development in Numerical methods for Turbomachinery Flows*. von Karman Institue for Fluid Dynamics, lecture Notes 2002-01.

SHARMA, O. & BUTLER, T. 1987 Predictions of endwall losses and secondary flows in axial flow turbine cascades. *Journal of Turbomachinery* **109**, 229–236.

SIEVERDING, C. 1985 Recent progress in the understanding of basic aspect of secondary flows in turbine blade passages. *Journal of Engineering for Gas Turbines and Power* **107**, 248–257.

SIMONEAU, R. & SIMON, F. 1993 Progress towards understanding and predicting heat transfer in the turbine gas path. *International Journal of Heat and Fluid Flow* **14**, 106–128.

SPENCER, M. & JONES, T. 1996 Endwall heat transfer measurements in an annular cascade of nozzle guide vanes at engine representative reynolds and mach numbers. *Journal of Heat and Fluid Flow* **17**, 139–147.

THOLE, K., RADOMSKY, R., KANG, M. & KOHLI, A. 1995 Enhanced heat transfer and shear stress due to high free-stream turbulence. *Journal of Turbomachinery* **117**, 418–424.

THOLE, K., RADOMSKY, R., KANG, M. & KOHLI, A. 2002 Elevated freesteam turbulence effects on heat transfer for a gas turbine vane. *International Journal of Heat and Fluid Flow* **23**, 137–147.

VERSTEEG, H. & MALALASEKERA, W. 1995 *An introduction to Computational Fluid Dynamics*. Addison Wesley Longman Ltd.

85

WILCOX, D. 1988 Reassessment of the scale-determining equation for advanced turbulence models. *AIAA Journal* **26**, 1299–1310.

WILCOX, D. 1993 *Turbulence Modeling for CFD*. Griffin Printing, Glendale.